Diese Arbeit wurde vorgelegt am
Lehrstuhl II für Mathematik

Robuste Optimierung von Zielpunktstrategien von Heliostaten in Solarturmkraftwerken

Robust Optimization of Aiming Strategies of Heliostats in Solar Tower Power Plants

Bachelorarbeit
Computational Engineering Science

August 2018

Vorgelegt von Presented by	Fynn Kepp Mauerstraße 71 52064 Aachen Matrikelnummer: 344700 fynn.kepp@rwth-aachen.de
Erstprüfer First examiner	Jun.-Prof. Dr. Christina Büsing Lehrstuhl II für Mathematik RWTH Aachen University
Externer Betreuer External supervisor	Dr. Pascal Richter Steinbuch Centre for Computing Karlsruhe Institute of Technology
Koreferent Co-Supervisor	M. Sc. Sascha Kuhnke Lehrstuhl II für Mathematik RWTH Aachen University

Eigenständigkeitserklärung

Hiermit versichere ich, dass ich diese Bachelorarbeit selbständig verfasst und keine anderen als die angegebenen Quellen und Hilfsmittel benutzt habe. Die Stellen meiner Arbeit, die dem Wortlaut oder dem Sinn nach anderen Werken entnommen sind, habe ich in jedem Fall unter Angabe der Quelle als Entlehnung kenntlich gemacht. Dasselbe gilt sinngemäß für Tabellen und Abbildungen. Diese Arbeit hat in dieser oder einer ähnlichen Form noch nicht im Rahmen einer anderen Prüfung vorgelegen.

Aachen, im August 2018

Fynn Vincent Kepp

Contents

1 Introduction

With renewable energy becoming more and more important globally [3], it is an important objective to increase the efficiency of renewable energy power plants.

A promising option for using renewable energy is concentrated solar power (CSP), whose thermal global capacity increased more than ten times since 2006 [3]. It uses the direct radiation of the sun to provide electric energy; this technology is not only environmentally friendly and sustained, it also provides electric energy in a highly scalable way and is able to compensate fluctuations in the available solar radiation by using heat storages.

Solar tower power plants are one way to use CSP. Mirrors in a frame equipped with a motor to track the sun, called heliostats, are grouped around a tower and concentrate the solar radiation onto its top end where the receiver is located. The concentrated solar power at the receiver is used to generate steam, which powers a turbine generating electricity.

The aiming strategies used to align the heliostats are of great importance. They have to ensure that the maximum of the possible heat flux is transferred to the receiver while no safety constrains are violated. To make the aiming strategies applicable to real power plants the latter has to especially hold true for uncertainties as tracking errors of the heliostats.

This bachelor thesis presents robust aiming strategies for the heliostats in solar tower power plants to increase their efficiency and the lifespan of the receiver. Solutions to align the heliostats in a way to obtain the maximum of the possible heat flux at the receiver while not violating any safety constraints that could damage it are demonstrated. Additionally an approach for obtaining desired heat flux distributions at the receiver is presented.

1.1 Outline of the work

At first an overview over the functioning principle of a solar tower power plant and the state of the art of aiming strategies for heliostats in such power plants is given.

In Section 2 we develop the optical model, which is used to determine the total heat flux distribution at the receiver consisting of the individual heat flux distributions of the heliostats. For that purpose we analyze the components of a real solar tower power plant and derive the mathematical model that we use for computing the distributions for a given plant setup afterwards.

In Section 3 we derive the deterministic aiming strategy as integer linear program (ILP). We take the receiver properties given as the maximum allowed heat flux per area, maximum heat flux gradients and the existence of a heat shield as well as clouds into account. As we do not consider uncertainties in the model description, we obtain an optimization model with a deterministic outcome.

In Section 4 we consider uncertainties in the aiming mechanism of the heliostats for the optimization model. Thus the deterministic model is extended to a robust model such that a robust aiming strategy is obtained. We analyze how these uncertainties have an effect on the receiver heat flux distribution, embed them into the deterministic model and derive the complete mixed integer linear programming (MILP) formulation of the robust aiming strategy.

In Section 5 we apply the aiming strategies we developed to the solar tower power plant PS10 in Spain. We use different sun positions, receiver properties and solver settings to obtain a variety of realistic application cases.

In Section 6 we draw the conclusion of the aiming strategies and give an outlook with possibilities to extend this work.

1.2 Functioning principle

The functioning principle of a typical solar tower power plant is visualised in Figure 1.

To provide electric energy, the heliostats concentrate the solar radiation onto a receiver, which transfers the heat to a medium (water, salt, air, sodium). If the medium is water, it evaporates through the heat and becomes steam. If the medium is another heat carrying fluid, it absorbs the heat from the receiver and exchanges it with a secondary cycle containing water, which then becomes steam. In both cases the steam drives a turbine. Its mechanical work is converted into electric energy by a generator. The steam water mixture leaving the turbine then is condensed by cooling it using water or air.

In order to provide electric energy even after the sundown or to provide a constant output of electric energy, the steam can be stored instead of being directly used to generate electric energy. Other heat carrying mediums can be stored in thermal storages before the heat is used to generate steam. Alternatively a gas turbine can compensate temporary fluctuations in the thermal energy projected towards the receiver (e.g. caused by clouds shading heliostats).

1.3 State of the art

There already exist different approaches for aiming strategies, which are outlined below:

- Ashley et al.[5] uses linear programming to obtain an optimal aiming strategy. Depending on the resolution of the receiver it provides optimal solutions close to real time. Heat flux gradients and uncertainties are not considered.

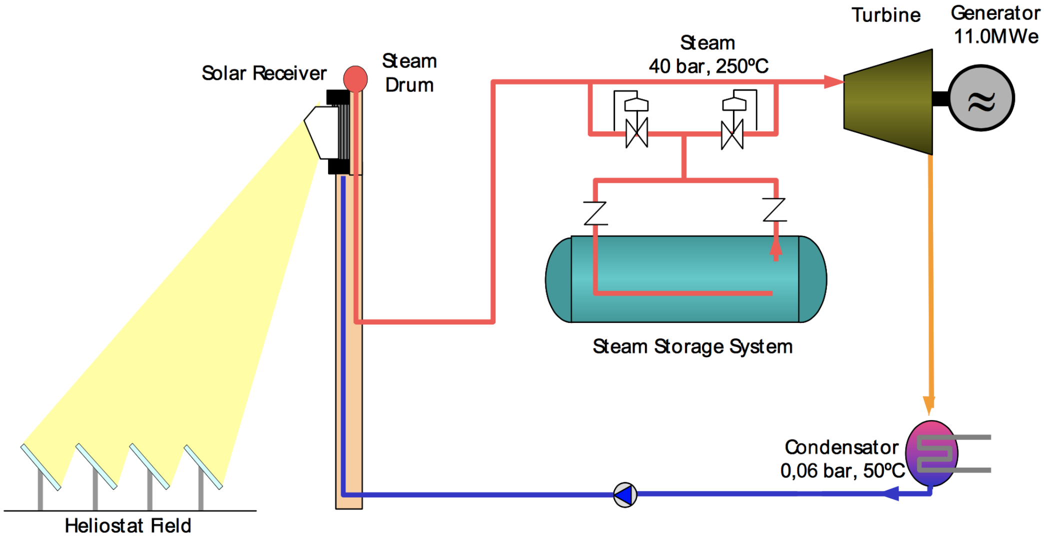

Figure 1: Functioning principle of the PS10 solar tower power plant in Spain. Source: [15]

- Astolfi et al.[6] proposes a method to reduce peak heat fluxes for up to 15% compared to other aiming point strategies in 120s computational time.
- Belhomme et al.[7] proposes a solution based on the ant colony optimization metaheuristic. This method is able to find solutions in up to 15 minutes while being up to 99% close to the optimal solution. Different types of receiver constraints as maximum heat fluxes or maximum heat flux gradients are considered.
- Besarati et al.[9] uses a genetic algorithm to homogenize the heat flux density over the receiver surface, meaning that peak heat fluxes are prevented.
- Dellin et al.[10] proposes a set of fixed aiming strategies in which the aim points of the heliostats are distributed in specific patterns. Its objective is to minimize thermal energy missing the receiver while also minimizing potential peak heat fluxes.

[5], [9] and [10] do not consider heat flux gradients at the receiver. Furthermore there is no work which takes into account uncertainties that can lead to deviation of heliostat heat flux distributions. As these effects can cause violations of safety constraints at the receiver, it is important to consider those when developing an optimal aiming strategy.

[6], [7] and [10] do not necessarily find an optimal aiming strategy due to being heuristic or being too generic per definition. While a good solution can be sufficient – especially when it can be computed fast – an optimal solution is preferable when it can be computed in a similar amount of time.

In this work we extend the approach from [5] and develop two aiming strategies formulated as an ILP or respectively as an MILP. The aiming strategies are applicable to arbitrary receiver geometries and determine the optimal aim point at the receiver for each heliostat in a solar tower power plant.

2 Optical model

The optical model is used to determine the heat flux distribution at the receiver. In this work we model that distribution by using the individual heat flux densities of the heliostats, the *images*, and aggregating them on top of each other. We look to compute these images for a given setup of heliostats, tower, outer shape of the receiver, sun position, points at which the heat flux is measured and points that can be targeted by the heliostats and to apply the images to the receiver.

To do that, we discuss different possibilities for generating heliostat images at first and then choose the method we use in this work. After that, we conceptually follow the path of the sun rays: We start by describing the properties of the sun, which are relevant for computing heliostat images. Continuing, we model the heliostats and lastly the receiver.

2.1 Methods for obtaining heliostat images

In the following two different ray tracing methods are presented.

2.1.1 Monte Carlo ray tracing

The Monte Carlo ray tracing method uses numerous rays that represent the rays coming from the sun. The path these rays take is traced: It ends if the ray does not get reflected at an obstacle and increases a ray counter of a subarea at the receiver if it is absorbed by it.

A ray hitting a mirror is reflected in the direction set by the orientation of the surface of the mirror. With a probability it might scatter or not get reflected at all. If a ray hits the receiver and does not get reflected at its surface (which is very likely due to the design of the receiver), it increases the counter of the region hit to indicate the heating of the surface. The higher that counter is, the larger is the heat flux hitting that subarea.

With ray tracing it is possible to create nearly physically correct simulations, as different errors as well as effects affecting the path of a ray like shading or blocking, which are outlined in Section 2.3, can be considered. The larger the number of generated rays is, the higher is the accuracy of the simulation due to the law or large numbers. The drawback is, that this method is computationally very expensive, as a very large number of rays has to be evaluated.

2.1.2 Convolution method

A faster but less accurate method is the use of error cones, where the probability of a ray hitting a specific area is represented by a circular Gaussian distribution. Its midpoint is the location, which originally was intended to be hit; its distribution size is defined by the errors taken into account and the distance the ray i.e. the cone travelled.

The heat flux density at every point of the cone can be evaluated analytically. With this approach it is possible to compute the heliostat images parallely at a relatively low computational cost; furthermore its implemenation is relatively simple. For these reasons this approach is used in this work.

2.2 Sun

2.2.1 Irradiation

The sun sends out solar radiation, which is a sum of direct and diffuse radiation. The first consists of the rays, which directly hit an obstacle as the ground or mirrors, the latter consists of the rays, which have been scattered. CSP plants can only use direct radiation as diffuse radiation cannot be concentrated.

The intensity of direct radiation is specified as the DNI (Direct Normal Irradiance) in $\mathrm{W/m^2}$, which can be measured on a surface normal to the direction of the rays sent out by the sun. We assume the DNI to be measured at ground level, so that attenuation of the irradiation from the sun at the ground by several effects of the atmosphere is already considered.

If a surface is not normal to the rays direction, the irradiance hitting that surface is reduced, because the same heat flux is spread over a larger area. This effect is known as cosine loss. The intensity I of the solar radiation considering cosine losses is computed as

$$I = \mathrm{DNI} \cdot \cos(\phi_i), \tag{1}$$

where ϕ_i is the incidence angle between the normal of the plane hit and the direction of the sun rays.

2.2.2 Sun position

For computing the direction of the sun rays we need to determine the position of the sun. This can be done with models as [12] that take the geographic location, date and time into account and express the position of the sun in polar coordinates using two angles:

- θ_{solar} is the zenith angle. The zenith is the elongation of the y-axis in Figure 2 i.e. an axis normal to the ground into the sky. The zenith angle is the angle between it and the sun. It is defined between $0°$ and $90°$.

- γ_{solar} is the azimuth angle, representing the angle between the sun's position projected onto a horizontal plane and the z-axis in Figure 2 i.e. an axis from south to north. It is $-90°$ for an directly eastern, $0°$ for a directly southern and $90°$ degrees for a directly western position.

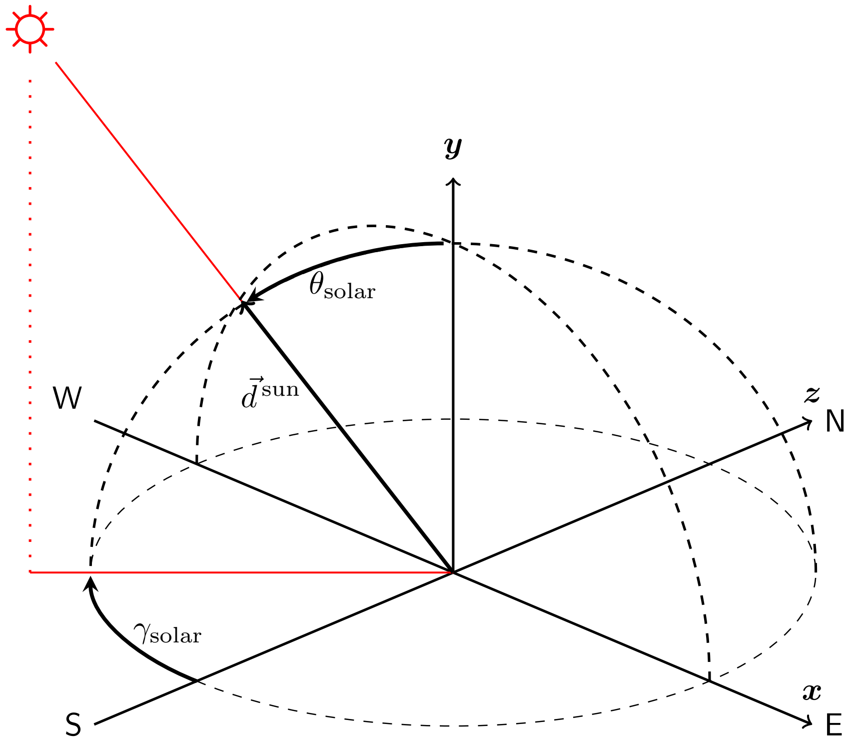

Figure 2: Position of the sun in dependancy of the angles γ_{solar} and θ_{solar}

With these angles known it is possible to describe the direction of the sun by the unit vector $\vec{d}^{\text{sun}}$ as

$$\vec{d}^{\text{sun}} = \begin{pmatrix} -\sin(\gamma_{\text{solar}}) \cdot \sin(\theta_{\text{solar}}) \\ \cos(\theta_{\text{solar}}) \\ -\cos(\gamma_{\text{solar}}) \cdot \sin(\theta_{\text{solar}}) \end{pmatrix} \tag{2}$$

for a three-dimensional Cartesian coordinate system where the x-axis is facing from west to east, the y-axis into the sky and the z-axis from south to north as given in Figure 2.

Note that $\vec{d}^{\text{sun}}$ has to be adjusted if the axes for the receiver are chosen differently. The axes in Figure 2 are consistent with the axes chosen for the receivers in Section 2.4.

2.2.3 Sun shape error

The sun causes the so-called sunshape error σ_{sunshape} that we have to consider later on as it can lead to reflected rays missing the receiver. The reason for this error is that the rays of the sun are not perfectly parallel but slightly fanned out due to the shape of the sun being a sphere and thus do not get reflected as intended. σ_{sunshape} is given by 2.51mrad [14] and stochastically independent.

2.3 Heliostats

2.3.1 Component description

The heliostats consist of a motor and a frame, which is holding one or several mirrors. Depending on the size of the power plant, the total mirror area of a heliostat can be between 1 and 140 m^2 [4]. The coating is made of a highly reflective material such as silver. Above that layer there are protective layers against weather conditions and dirt [1].

The mirrors are curved in a way, that the reflected solar radiation is concentrated at the desired point, which is at the receiver surface. This results in heliostats closer to the tower having a stronger curvature than those further away. As the sun moves during the day, the mirrors have to be moved as well. To track the sun as well as possible in order to minimize cosine losses, the tracking is usually done along a vertical and a horizontal axis, which is called biaxial tracking.

2.3.2 Set of heliostats

We combine the heliostats in a solar tower power plant in the set H. It is a listing given by

$$H = \{1, ..., n_h\}, \tag{3}$$

where n_h is the number of heliostats.

2.3.3 Heliostat errors

We model the following errors for a heliostat $h \in H$, which can lead to rays eventually missing the receiver.

- The optical error $\sigma^h_{\text{optical}}$ caused by the surface(s) of the mirror(s) not being perfectly curved and having small roughnesses. We assume $\sigma^h_{\text{optical}}$ to be known and stochastically independent for all $h \in H$.

  We consider σ_{optical} in the optical model for computing the heliostat images, because it is a result of the manufacturing process and does not change at all; neither over time nor due to change of another quantity.

- The horizontal and vertical tracking errors $\sigma^h_{\text{tracking,hor}}$ and $\sigma^h_{\text{tracking,ver}}$ caused by several effects such as limited accuracy of the motor or imperfections in the determination of the reference position for the tracking mechanic or in the construction of the frame and the tracking system that can lead to the tracking mechanism as a whole being inaccurate. As most heliostats in solar tower power plants are tracked biaxially to account for changing values of γ_{solar} and θ_{solar}, we consider horizontal and vertical tracking errors $\sigma^h_{\text{tracking,hor}}$ and $\sigma^h_{\text{tracking,ver}}$.

Contrary to the optical error, the horizontal and vertical tracking errors are going to be handled as uncertainties in Section 4. Not only may they change over time or depending on the aim point the heliostat is targeting but additionally they behave in a non-Gaussian way [11].

2.3.4 Shading and blocking

The following effects can lead to changes of the heliostat images.

- **Shading:** If the radiation of the sun does not or only partly hit heliostats due to obstacles being in the way, we speak of shading. The images of the corresponding heliostats are zero or respectively partly zero, as no radiation is reflected from their shaded areas.

  Shading can be induced by the solar tower itself or by clouds by casting their shadows onto the heliostat field. Additionally heliostats can shade each other, when they are aligned in such a way, that those closer to the sun cast a shadow on those further back.

- **Blocking:** If radiation is reflected by a heliostat, but hits another one on its path to the receiver, the image is also zero at the corresponding area. This effect is known as blocking.

For the sake of simplicity we neglect shading and blocking in this work.

2.3.5 Incidence angle

The incidence angle $\phi_i^{h,a}$ for the heliostat $h \in H$ and the targeted point a at the receiver surface is located between the normal $\vec{n}^{h,a}$ of the heliostat hit and the vector $\vec{d}^{\text{sun}}$ representing the position of the sun as seen from every heliostat or respectively the direction vector $\vec{d}^{h,a}$ pointing from the heliostat onto a. A visualisation of this is shown in Figure 3.

$\vec{d}^{\text{sun}}$ is obtained by using Equation (2), $\vec{d}^{h,a}$ is computed by

$$\vec{d}^{h,a} = \vec{p}^a - \vec{p}^h, \tag{4}$$

with $\vec{p}^a$ and $\vec{p}^h$ being the known position vectors of the a and h.

Note that the normal $\vec{n}^{h,a}$ of the heliostat h is exactly between $\vec{d}^{\text{sun}}$ and $\vec{d}^{h,a}$, as the heliostat is aligned in a way that the irradiation is projected towards a. For this reason we can compute $\phi_i^{h,a}$ as half the angle between $\vec{d}^{\text{sun}}$ and $\vec{d}^{h,a}$ as

$$\phi_i^{h,a} = \frac{1}{2} \cdot \cos^{-1}\left(\frac{\vec{d}^{\text{sun}} \cdot \vec{d}^{h,a}}{||\vec{d}^{h,a}||_2}\right). \tag{5}$$

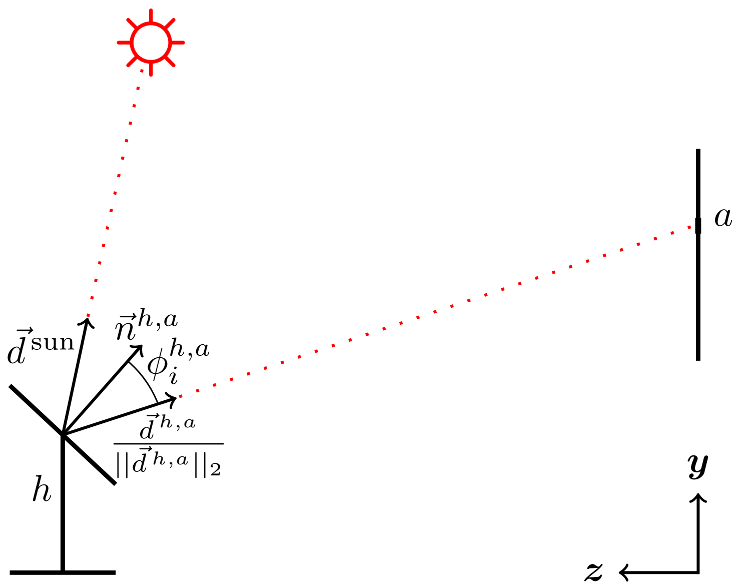

Figure 3: Computation of $\phi_i^{h,a}$ by using $\vec{d}^{\text{sun}}$ and $\vec{d}^{h,a}$.

2.3.6 Atmospheric attenuation

The heat flux reflected by a heliostat is reduced by the atmospheric attenuation. The larger the distance between the heliostat $h \in H$ and the targeted point a at the receiver surface, the larger is the effect of the atmospheric attenuation as the ray travels a larger distance through the atmosphere.

The atmospheric attenuation $\eta_{\text{aa}}^{h,a}$ is computed by using different approaches depending on the distance $d^{h,a}$ between h and a. The distance in meter is computed by using the Euclidean norm of the vector $\vec{d}^{h,a}$ from Equation (4) i.e.

$$d^{h,a} = ||\vec{d}^{h,a}||_2. \tag{6}$$

For distances smaller than 1000m we use a polynomial approach as proposed in [13]; for distances larger than a 1000m up to about 40000m we use an exponential approach as proposed in [16]. The constants for both approaches are taken from [18].

With the distance being known, we then can compute $\eta_{\text{aa}}^{h,a}$ as

$$\eta_{\text{aa}}^{h,a} = \begin{cases} 0.99321 - 1.176 \cdot 10^{-4} \cdot d^{h,a} + 1.97 \cdot 10^{-8} \cdot d^{h,a^2} & \text{for } d^{h,a} \leq 1000 \\ \exp(-1.106 \cdot 10^{-4} \cdot d^{h,a}) & \text{for } d^{h,a} > 1000. \end{cases} \quad (7)$$

2.3.7 Beam power

The total amount of heat being reflected by a heliostat $h \in H$ that targets point a at the receiver surface, is the beam power $P^{h,a}$. It depends on the irradiance $I^{h,a}$ hitting the heliostat, the atmospheric attenuation $\eta_{\text{aa}}^{h,a}$, the area of the mirror surface A^h and its reflectivity r^h.

If a heliostat consists of several mirrors, we assume that A^h is obtained by summing up the area of its mirrors. The reflectivity $r^h \in [0, 1]$ represents the amount of incoming radiation that is being reflected by heliostat h. $r^h = 0$ corresponds to no reflection, while $r^h = 1$ means, that everything of the incoming radiation is reflected.

By using Equation (1) we can compute the beam power $P^{h,a}$ of h targeting a as

$$P^{h,a} = I^{h,a} \cdot \eta_{\text{aa}}^{h,a} \cdot A^h \cdot r^h = \text{DNI} \cdot \cos(\phi_i^{h,a}) \cdot \eta_{\text{aa}}^{h,a} \cdot A^h \cdot r^h. \quad (8)$$

2.3.8 Original HFLCAL method

The HFLCAL (Heliostat Field Layout CALculation) method [19] is an analytic method for obtaining heliostat images. It approximates the heat flux density $\tilde{Q}''^{h,a}_{x,y}$ in $\frac{\text{W}}{\text{m}^2}$ at the receiver for a heliostat $h \in H$ targeting the so called aim point a on the receiver surface as follows:

$$\tilde{Q}''^{h,a}_{x,y} = \frac{P^{h,a}}{2\pi\tilde{\sigma}^{h,a}_{\text{effective}}} \cdot \exp\left(-\frac{x^2 + y^2}{2\tilde{\sigma}^{h,a}_{\text{effective}}}\right) \quad (9)$$

- x and y are the distances of the currently considered infinitesimal element from a, which is located at $(0, 0)$, in the plane of the receiver in x- and y- i.e. in horizontal and in vertical direction.
- $P^{h,a}$ is the beam power from Equation (8), i.e. the amount of heat being reflected from the heliostat, depending on the heliostat, the targeted aim point and the position of the sun.
- $\tilde{\sigma}^{h,a}_{\text{effective}}$ is the effective error defining the distribution size.

The effective error is defined as

$$\tilde{\sigma}^{h,a}_{\text{effective}} = \frac{d^{h,a} \cdot \sigma^h_{\text{total}}}{\sqrt{\cos(\phi^{h,a})}} \quad (10)$$

with $d^{h,a}$ being the distance between the heliostat and the targeted aim point at the receiver as defined in Equation (6). The effective error and thus the size of the heliostat image becomes larger for an increasing distance $d^{h,a}$.

The total error σ^h_{total} is defined as the Euclidean norm of the beforehand known/approximated errors, hence it is computed as

$$\sigma^h_{\text{total}} = \sqrt{(\sigma^h_{\text{optical}})^2 + \sigma^2_{\text{sunshape}}}. \tag{11}$$

We can summarize these errors, because they all are stochastically independent and have the same influcence on the distribution, increasing its size.

The incident angle $\phi^{h,a}$ is the angle between the incoming reflected radiation from the heliostat and the normal of the receiver surface at the hit receiver point projected onto the ground, i.e. the incident angle in x-direction. If a rectangular receiver is aligned in a way, that its normal points northern and the reflected radiation is sent from a heliostat which is located perfectly northern without offset towards the western or eastern direction as well, than this angle is zero otherwise it becomes a value between zero and 90 degrees depending on the heliostats position.

2.4 Receiver

2.4.1 Component description

The task of the receiver is to absorb the thermal energy projected onto it by the heliostats and to transfer it to the heat carrying fluid.

To do that there exist different design types of receivers for solar tower power plants depending on the size of the plant, the structure of the heliostat field and the type of the heat carrying medium. The design type of the receiver influences its outer shape and the material used.

For the outer shape there exist two different groups of receivers in commercially operating solar tower power plants: the cavity and the external receiver. Cavity receivers are curved towards the inner of the tower to minimize heat losses through radiation and especially convection [15] as they are sheltered from wind. External receivers are attached at the outside of the tower and thus usually have higher heat losses.

Different shapes for receivers are possible. These can be cylindrical or spherical for cavity receivers and rectangular or cylindrical around the tower for external receivers. The latter are especially used in larger power plants, where the tower is usually surrounded by the heliostat field. Such an cylindrical external receiver is shown in Figure 4.

The material has to be able to withstand high temperatures as well as relativly high temperature gradients and efficiently transfer the concentrated heat to the medium

Figure 4: The cylindrical external receiver of the *Gemasolar* power plant in Spain. Source: [2]

flowing through the receiver, while still obtaining a long lifespan.

Usually a heat shield is attached at the edges of the receiver to protect the solar tower from heat fluxes missing the receiver. It is also made of a material that can withstand high temperatures and temperature gradients such as ceramic. As it does not transfer the heat to the heat carrying medium flowing at the inside of the receiver, it is not actively cooled, which usually means that it cannot withstand heat flux intensities as high as the receiver.

2.4.2 Receiver model

We model the receiver by discretizing its surface and storing the heat flux values at the subareas resulting from the discretization process into matrices. Rectangular receivers already have a shape, which can easily be described by a matrix. Cylindric receiver types are flattened out, so they form a rectangle, which then can be described as a matrix as well. We model rectangular external, cylindric cavity and cylindric external receivers.

As already described we obtain the total receiver heat flux distribution by aggregating the images of every heliostat. A visual representation of such a receiver heat flux distribution is given in Figure 5.

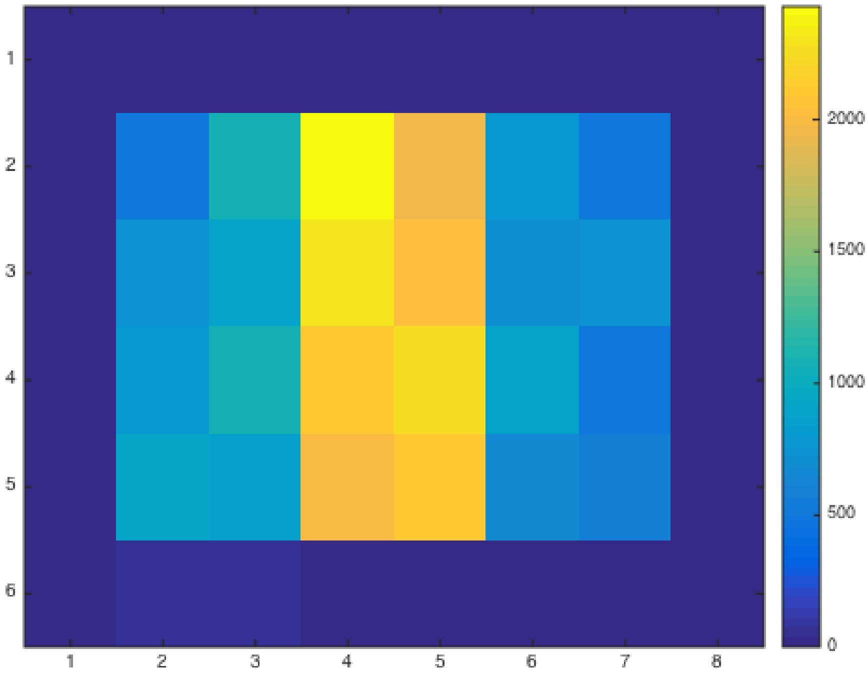

Figure 5: Heat flux distribution in kW at each point for 6 $\times$ 4 receiver points and one heat shield point to each side for a 14m $\times$ 12m cavity receiver.

2.4.3 Measurement points

We are interested in the heat flux value at each point of the receiver heat flux distribution. As we 'measure' our simulated heat fluxes at these points, they are called measurement (index m) points.

In this work we will use the tuple (i, j) to refer to them. The set M containing the measurement points is given by

$$M = \{(i, j) : i \in \{1, ..., n_{m,x}\}, j \in \{1, ..., n_{m,y}\}\}, \tag{12}$$

where $n_{m,x}$ and $n_{m,y}$ are the number of horizontal and vertical measurement points. The numeration starts at the bottom left corner of the receiver. For the external receiver any horizontal coordinate for the start of the numeration can be chosen. i is the horizontal, j the vertical index.

When deriving aiming strategies based on optimization later on, we are going to use matrices containing the constraints for the optimization as for instance the maximum allowed heat flux values at each receiver point. These matrices have to be determined by thermodynamic simulations done for the specific receiver and are assumed to be given. The resolution of those simulations directly defines the number of entries in the constraint matrices and thus also the number of measurement points.

If a specific thermodynamical simulation is not needed – for instance due to the heat flux limit being constant for the whole receiver – or if one has the possibility to do such simulations with an arbitrary number of distribution points it is also possible to choose the number of measurement points.

2.4.4 Aim points

Additionally to the measurement points we need the mentioned aim points (index a). These are the points, which can be targeted by the heliostats. When tracking errors are neglected, the focus point of the heat flux distribution is at the targeted aim point. The number of aim points can be chosen arbitrarily, but to obtain an optimal discretization one has to use a certain ratio of measurement to aim points as described in the next paragraph.

The set A containing the aim points is analogously given by

$$A = \{(i, j) : i \in \{1, ..., n_{a,x}\}, j \in \{1, ..., n_{a,y}\}\}, \tag{13}$$

where $n_{a,x}$ and $n_{a,y}$ are the number of horizontal and vertical aim points. The indices i and j are analogous to the indices for the measurement points.

2.4.5 Optimal discretization

For the sake of simplicity we use an equidistant discretization. It is recommended – even though it is not mandatory – to choose the number of aim points in such a way, that $n_{m,x}$ and $n_{m,y}$ are multiples of the number of aim points $n_{a,x}$ and $n_{a,y}$ in the respective directions if a thermodynamic simulation with a fixed resolution is given.

Alternatively – if possible – one can define the resolution of the thermodynamic simulation, which determines the number of measurement points in the horizontal and vertical direction, in such a way, that $n_{m,x}$ and $n_{m,y}$ are multiples of the chosen number of aim points $n_{a,x}$ and $n_{a,y}$ in the respective directions.

If it holds that

$$\frac{n_{m,x}}{n_{a,x}} \in \mathbb{N}$$
$$\frac{n_{m,y}}{n_{a,y}} \in \mathbb{N},$$

we obtain the most accurate results as the local heat flux distribution of a heliostat targeting a specific aim point is represented by the heat flux values of the measurement points positioned around the targeted aim point.

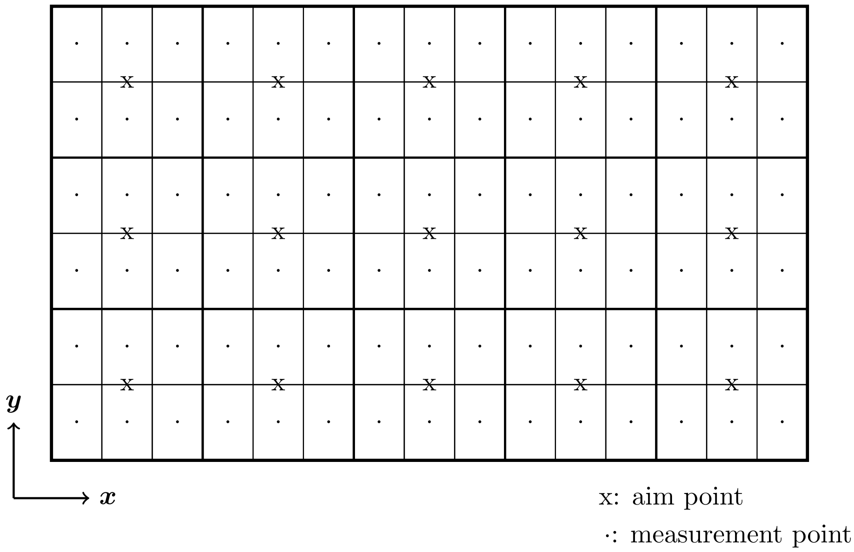

Figure 6: Discretization of a rectangular receiver with $n_{a,x} = 5$, $n_{a,y} = 3$, $n_{m,x} = 15$ and $n_{m,y} = 6$

2.4.6 Discretization of receiver types

Rectangular external receiver The shape of a rectangular external receiver is given by a rectangle with width w_{rec} and height h_{rec}. Usually the surface of the receiver is tilted towards the ground with an angle θ_{rec} to minimize heat flux losses through incident angles in the vertical direction. The origin of the coordinate system is defined at the midpoint of the solar tower at ground level. The axes are defined as shown in Figure 7.

For the known quantities of the solar tower the Cartesian coordinates of the measurement and aim points obtained for an equidistant discretization are given by

$$x_{p(i,j)} = \frac{w_{\text{rec}}}{2} - \frac{w_{\text{rec}}}{n_{p,x}} \cdot (i - \frac{1}{2}) \tag{14}$$

$$y_{p(i,j)} = h_{\text{tower}} - h_{\text{top}} - h_{\text{rec}} + \cos(\theta_{\text{rec}}) \cdot \frac{h_{\text{rec}}}{n_{p,y}} \cdot (j - \frac{1}{2}) \tag{15}$$

$$z_{p(i,j)} = w_{\text{tower}}/2 + \sin(\theta_{\text{rec}}) \cdot \frac{h_{\text{rec}}}{n_{p,y}} \cdot (j - \frac{1}{2}), \tag{16}$$

where p either represents m or a.

Cylindric cavity receiver The shape of a cylindrical cavity receiver is given by the inner surface of half a cylinder with height h_{rec} and diameter d_{rec}. The origin of the coordinate system is defined at the midpoint of the lower edge of the solar tower. The axes are defined as shown in Figure 8.

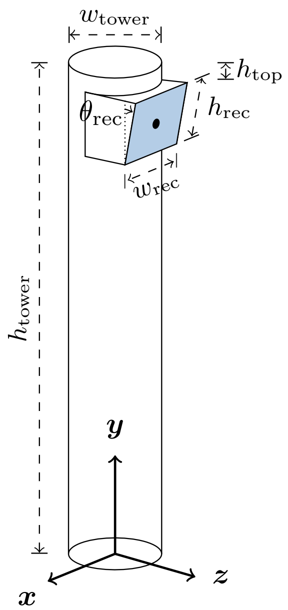

Figure 7: Model of a rectangular external receiver. Source: [17]

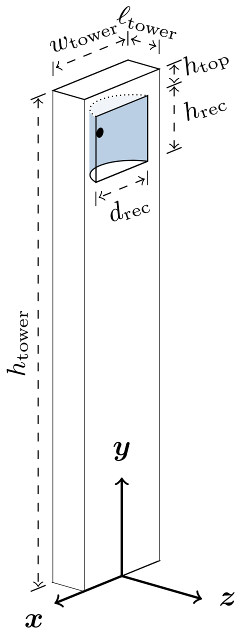

Figure 8: Model of a cylindrical cavity receiver. Source: [17]

For the known quantities of the solar tower the Cartesian coordinates of the measurement and aim points obtained for an equidistant discretization are given by

$$x_{p(i,j)} = -\frac{d_{\text{rec}}}{2} \cdot \cos\left(\tfrac{180}{n_{p,x}} \cdot (n_{p,x} - i + \frac{1}{2})\right) \tag{17}$$

$$y_{p(i,j)} = h_{\text{tower}} - h_{\text{top}} - h_{\text{rec}} + \frac{h_{\text{rec}}}{n_{p,y}} \cdot (j - \frac{1}{2}) \tag{18}$$

$$z_{p(i,j)} = -\frac{d_{\text{rec}}}{2} \cdot \sin\left(\tfrac{180}{n_{p,x}} \cdot (n_{p,x} - i + \frac{1}{2})\right), \tag{19}$$

where p either represents m or a.

Cylindric external receiver The shape of a cylindrical external receiver is given by the outside of a cylinder with height h_{rec} and diameter d_{rec} without its bottom and top area. The origin of the coordinate system is defined at the midpoint of the solar tower at ground level. The axes are defined as shown in Figure 9. The direction of the x- and z axis can be chosen arbitrarily as long as they are parallel to the ground.

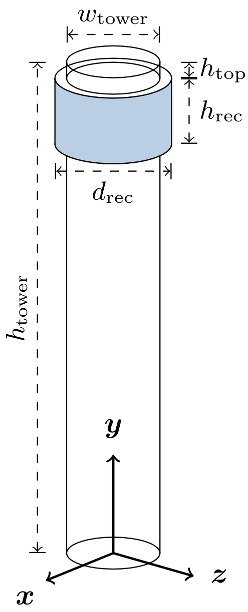

Figure 9: Model of a cylindrical external receiver. Source: [17]

For the known quantities of the solar tower the Cartesian coordinates of the measurement and aim points obtained for an equidistant discretization are given by

$$x_{p(i,j)} = \frac{d_{\text{rec}}}{2} \cdot \cos\left(\tfrac{360}{n_{p,x}} \cdot (i - 1)\right) \tag{20}$$

$$y_{p(i,j)} = h_{\text{tower}} - h_{\text{top}} - h_{\text{rec}} + \frac{h_{\text{rec}}}{n_{p,y}} \cdot (j - \frac{1}{2}) \tag{21}$$

$$z_{p(i,j)} = \frac{d_{\text{rec}}}{2} \cdot \sin\left(\tfrac{360}{n_{p,x}} \cdot (i - 1)\right), \tag{22}$$

where p either represents m or a.

2.5 Computing heliostat images

2.5.1 Integrating the heat flux

To obtain the total heat flux of one heliostat, we have to integrate a heat flux density function as given by Equation (9), which results in

$$\int_{-\infty}^{\infty}\int_{-\infty}^{\infty} \tilde{Q}''^{h,a}_{x,y}\,\mathrm{d}x\mathrm{d}y = \int_{\mathbb{R}^2} \tilde{Q}''^{h,a}_{x,y}\,\mathrm{d}A = P^{h,a}. \tag{23}$$

As the receiver surface is discrete rather than continuous we are looking to compute the heat flux at the area around the measurement points. To do that we evaluate Equation (9) at the coordinates of the measurement points (x, y) and scale it by the size of the area around that measurement point

$$\tilde{Q}^{h,a}_{x,y} = \tilde{Q}''^{h,a}_{x,y} \cdot A_m, \tag{24}$$

which is a two-dimensional midpoint quadrature rule.

2.5.2 Adapted HFLCAL method

We need to ensure that no safety constrains are violated when using an aiming strategy later on. For this reason we also have to make sure, that the heliostat images are as accurate as possible.

When using the incident angle in x-direction like an error amplification in Equation (10), we increase the width of the image in the x and y dimension, meaning we increase the diameter of the circular Gaussian distribution. When e.g. looking at heliostat images projected onto a rectangular receiver, we notice however, that the projected image is an ellipse and not a circle and that it not only depends on the incident angle in x- but also the y-direction.

For this reason we use an adapted version of this method to compute the images of the heliostats, in which we take the projections onto the receiver surface into account and consider the incidence angles in the x- and the y-direction. The incident angle in the y-direction is the angle between the incoming reflected radiation from the heliostat and the normal of the receiver surface at the hit receiver point projected onto the y-z-plane.

For the adapted version of the HFLCAL method we define $\sigma^{h,a}_{\text{effective}}$ as

$$\sigma^{h,a}_{\text{effective}} = d^{h,a} \cdot \sigma^{h}_{\text{total}} \tag{25}$$

and do the projection onto the surface of the receiver separately.

The projection process consists of two steps: Firstly we will use the distances (x_o, y_o), which we from now will call offsets, by projecting the actual distances (x, y) between

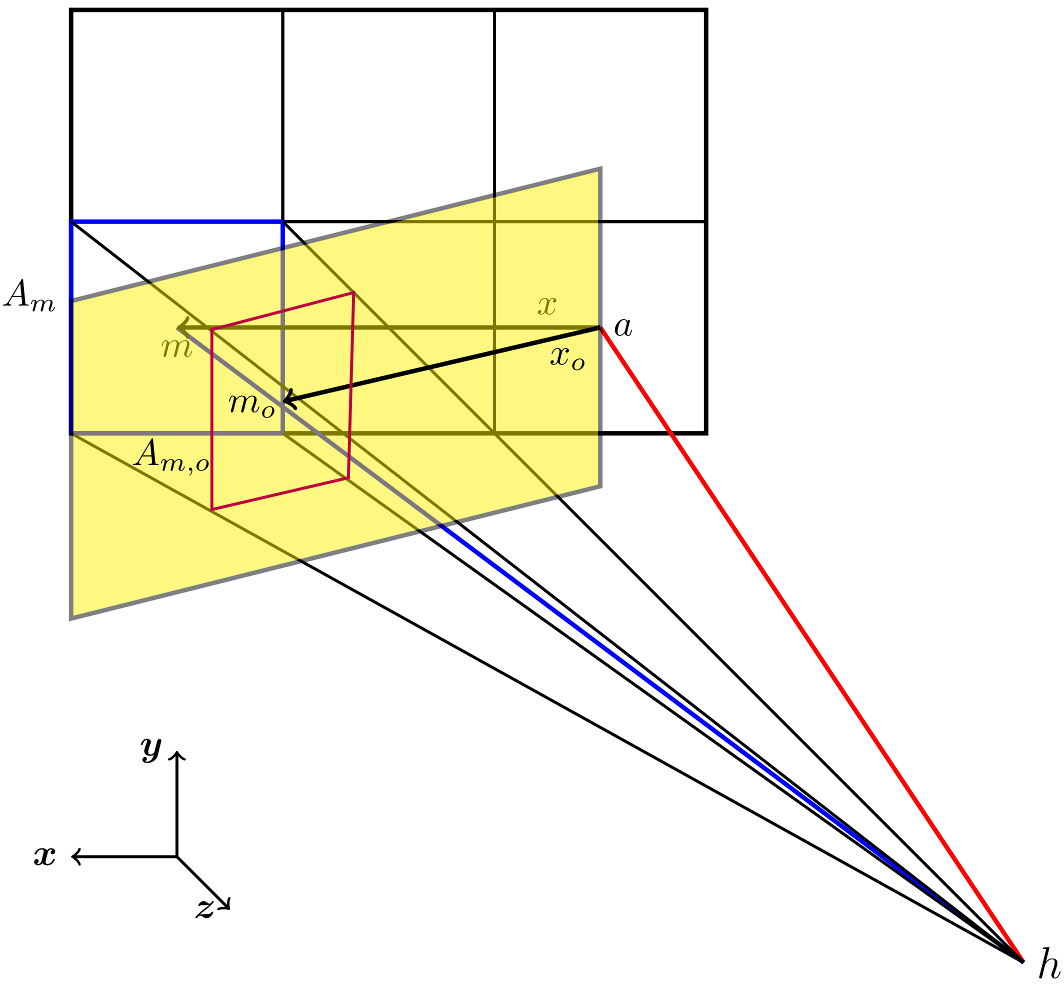

Figure 10: Projection process for $\phi_x > 0$ and $\phi_y = 0$. We use the offset x_o instead of the distance x to compute the heat flux at measurement point m when heliostat h targets aim point a and scale the intensity by the factor $\frac{A_{m,o}}{A_m}$.

the considered measurement and aim point onto a plane normal to the radiation of the heliostat.

Secondly we will adjust the heat flux intensity by projecting the area A_m around the considered measurement point onto said plane normal to the radiation of the heliostat, obtaining $A_{m,o}$ and using the ratio between projected and unprojected area $\frac{A_{m,o}}{A_m}$ to scale the heat flux intensity.

The heat flux density of a heliostat for the respective offsets is given by

$$Q''^{h,a}_{x,y} = \frac{P^{h,a}}{2\pi\sigma^{h,a}_{\text{effective}}} \cdot \exp(-\frac{x_o^2 + y_o^2}{2\sigma^{h,a}_{\text{effective}}}) \cdot \frac{A_{m,o}}{A_m}, \tag{26}$$

where we have to determine the offsets (x_o, y_o) and the projected area $A_{m,o}$ in respect of the distances (x, y) and the incidence angles. The equations needed for the projection process are derived in Section 2.5.3, the computation of the heliostat images as a whole for the known three receiver types is explained in the Sections 2.5.4, 2.5.5 and 2.5.6.

The total heat flux hitting a measurement point positioned at (x, y) then can be computed by numerically integrating Equation (26) as done in Equation (24) for the original HFLCAL approach. We obtain

$$Q_{x,y}^{h,a} = Q_{x,y}^{\prime\prime h,a} \cdot A_m, \tag{27}$$

which simplifies to

$$Q_{x,y}^{h,a} = \frac{P^{h,a}}{2\pi\sigma_{\text{effective}}^{h,a}} \cdot \exp\left(-\frac{x_o^2 + y_o^2}{2\sigma_{\text{effective}}^{h,a}}\right) \cdot A_{m,o}. \tag{28}$$

2.5.3 Distorted heliostat image matrix

In this section we derive the projection process for a point at the receiver plane onto a plane parallel to the heliostat.

As defined in Section 2.4.2 the x-axis is parallel to the receiver plane, while the z-axis points towards the heliostat field being normal to the x-axis. For a cylindric external receiver the x- and z-axis can be chosen arbitrarily. We assume that the Carthesian coordinates of the aim points and the heliostat thus that the distances $d_x^{h,a}$, $d_y^{h,a}$ and $d_z^{h,a}$ in the x, y and z dimension from every heliostat to the targeted aim point are known. With that knowledge we can compute $\phi_x^{h,a}$ and $\phi_y^{h,a}$ by

$$\phi_x^{h,a} = \tan^{-1}\left(\frac{d_x^{h,a}}{d_z^{h,a}}\right) \quad \text{and} \tag{29}$$

$$\phi_y^{h,a} = \tan^{-1}\left(\frac{d_y^{h,a}}{d_z^{h,a}}\right), \tag{30}$$

which has to be done for every heliostat once per aim point.

Our aim is to compute the offsets $(x_o^{h,a,m}, y_o^{h,a,m})$ to use them in Equation (26) or respectively Equation (28) to compute the intensity of the heat flux at measurement point $m \in M$ when heliostat $h \in H$ targets aim point $a \in A$. These offsets depend on the incidence angles $\phi_x^{h,a}$ and $\phi_y^{h,a}$ and the distances between the measurement points and the aim points, which are given by $x_r^{a,m}$ and $x_l^{a,m}$ (right and left) in the x- and by $y_u^{a,m}$ and $y_l^{a,m}$ (upper and lower) in the y-direction. In the following we derive the equations for the x-direction; the equations in y-direction are obtained analogously when exchanging the index x by y.

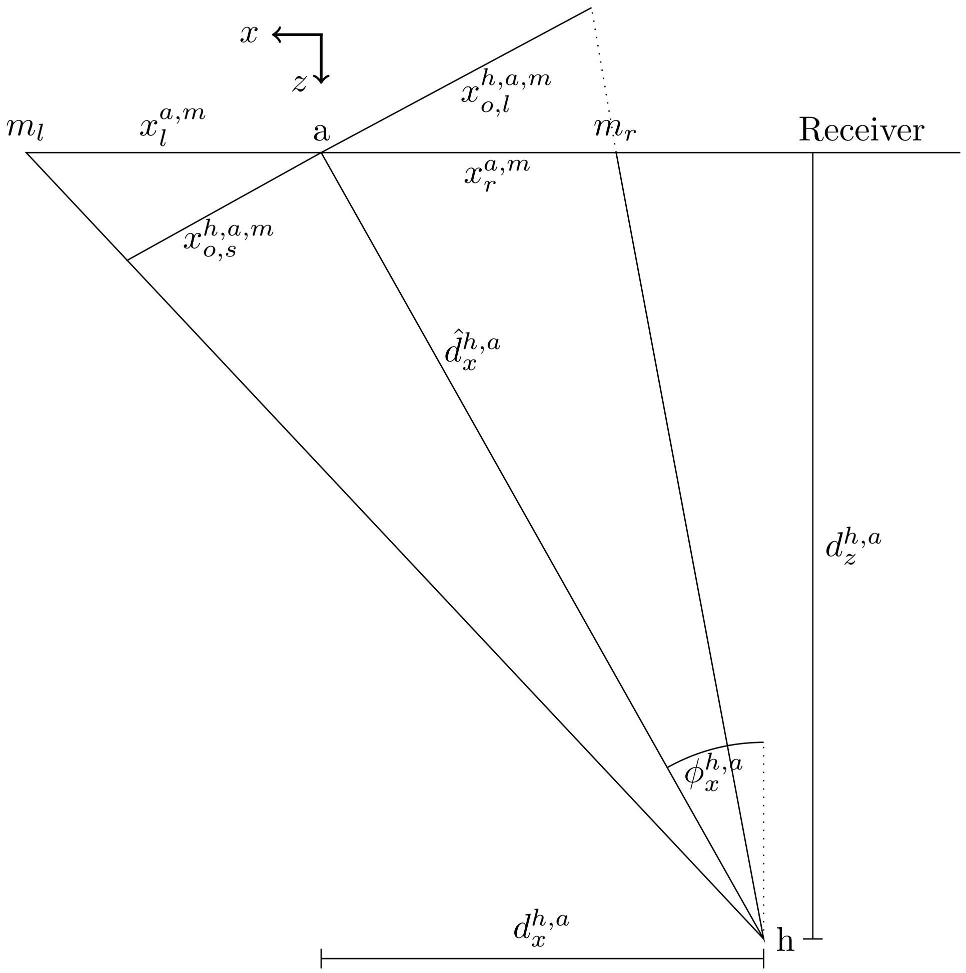

Figure 11: Trigonometry of the offset for the x-z-plane from a heliostat that is positioned to the right side of the targeted aim point

We use two representative measurement points as shown in Figure 11. m_l is positioned with the distance $x_l^{a,m}$ on the left, m_r with the distance $x_r^{a,m}$ on the right of the targeted aim point a. Depending on the position of the heliostat relative to the aim point we have to use the longer (index l) or shorter (index s) offset in the respective directions.

At first we want to determine the longer offset $x_{o,l}^{h,a,m}$, which is always going to be on the side of the targeted aim point where the heliostat is positioned. We use Figure 12 and determine the auxilary variable $\hat{x}_{o,l}^{h,a,m}$ to

$$\hat{x}_{o,l}^{h,a,m} = \cos(\phi_x^{h,a}) \cdot x_r^{a,m},$$

from where we can compute $x_{o,l}$ as

$$x_{o,l}^{h,a,m} = \frac{\hat{d}_x^{h,a}}{\hat{d}_x^{h,a} - \sin(\phi_x^{h,a}) \cdot x_r^{a,m}} \cdot \hat{x}_{o,l}^{h,a,m} = \frac{\hat{d}_x^{h,a} \cdot \cos(\phi_x^{h,a}) \cdot x_r^{a,m}}{\hat{d}_x^{h,a} - \sin(\phi_x^{h,a}) \cdot x_r^{a,m}} \tag{31}$$

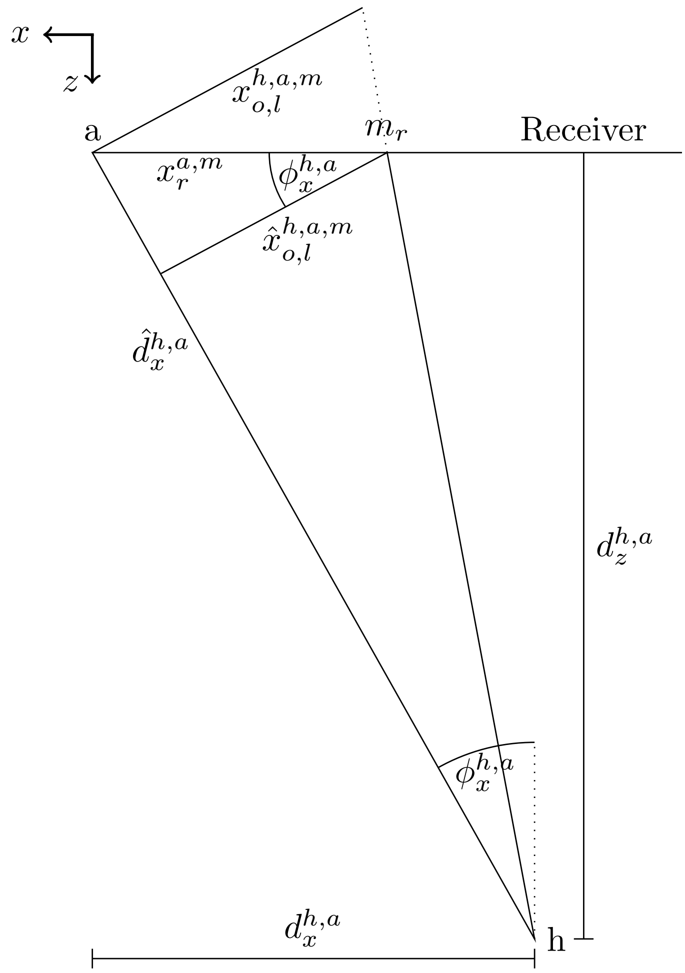

Figure 12: Right part of the trigonometry of the longer offset in the x-z-plane for a heliostat that is positioned to the right hand side of the targeted aim point

with $\hat{d}_x^{h,a} = \sqrt{{d_x^{h,a}}^2 + {d_z^{h,a}}^2}$.

For the shorter offset we use Figure 13 and determine $\hat{x}_{o,s}^{h,a}$ to

$$\hat{x}_{o,s}^{h,a,m} = \cos(\phi_x^{h,a}) \cdot x_l^{a,m},$$

from where we can compute $x_{o,s}^{h,a,m}$ as

$$x_{o,s}^{h,a,m} = \frac{\hat{d}_x^{h,a}}{\hat{d}_x^{h,a} + \sin(\phi_x^{h,a}) \cdot x_l^{a,m}} \cdot \hat{x}_{o,s}^{h,a,m} = \frac{\hat{d}_x^{h,a} \cdot \cos(\phi_x^{h,a}) \cdot x_l^{a,m}}{\hat{d}_x^{h,a} + \sin(\phi_x^{h,a}) \cdot x_l^{a,m}}. \tag{32}$$

Analogously the same equations hold if a heliostat is positioned to the left side of the targeted aim point. In that case the indices s and l are swapped, as the the shorter and longer sides of the offset are swapped as well respectively.

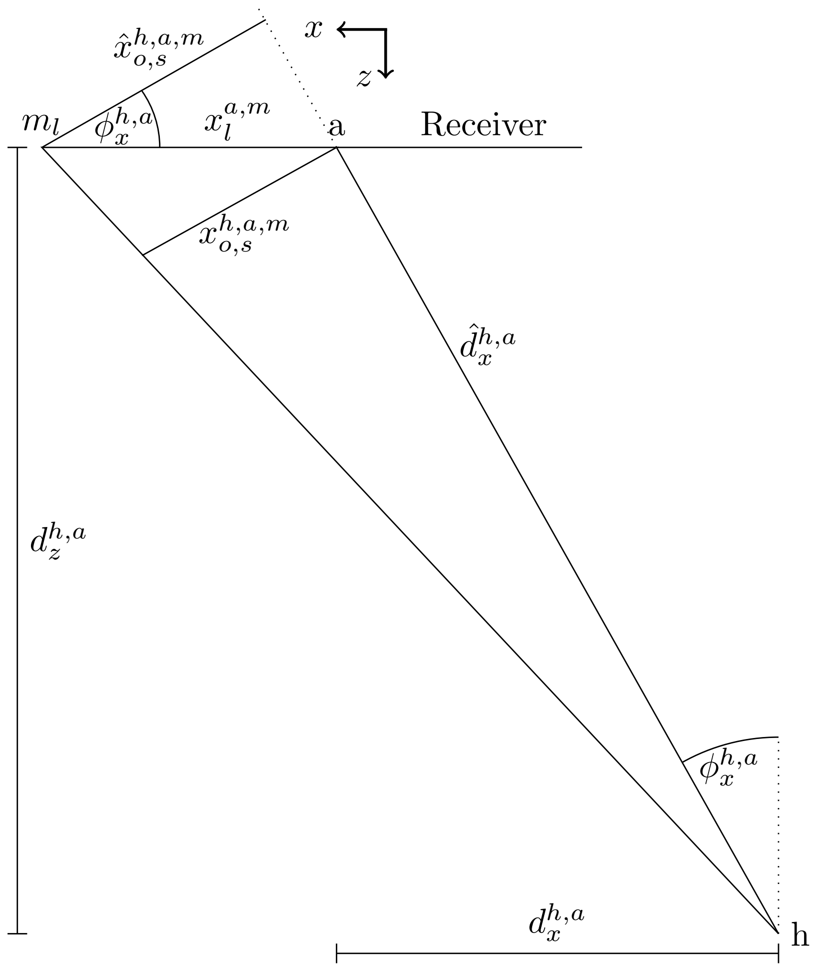

Figure 13: Left part of the trigonometry of the shorter offset in the x-z-plane for a heliostat that is positioned to the right hand side of the targeted aim point

2.5.4 Rectangular external receiver

For projecting a heliostat image onto a rectangular receiver we need to determine the cartesian coordinates of the measurement and aim points. With those being known, we can compute the areas around the measurement points and the distances between measurement and aim points, project them into the heliostat plane and finally compute the heat fluxes.

1 The Cartesian coordinates of the measurement points are computed by using the Equations (14) to (16) with $n_{m,x}$ and $n_{m,y}$.

2 The Cartesian coordinates of the aim points are computed using the Equations (14) to (16) with $n_{a,x}$ and $n_{a,y}$.

3 The distances Δx and Δy between the measurement points and the aim points are computed trivially by

$$\Delta_x = x_{m(i,j)} - x_{a(i,j)} \quad \text{and} \tag{33}$$

$$\Delta_y = \sqrt{(y_{m(i,j)} - y_{a(i,j)})^2 + (z_{m(i,j)} - z_{a(i,j)})^2}. \tag{34}$$

4 The offsets $x_o^{h,a,m}$ and $y_o^{h,a,m}$ (respectively long or short, depending on the position of the heliostat relative to the aim point) are computed by using the Equations (31) and (32) with the distances Δ_x and Δ_y from **3**. If $\alpha_r > 0$, we have to use the effective incident angle in y-direction $\phi_{y,\text{effective}}^{h,a}$ instead of $\phi_y^{h,a}$. The effective incident angle in y-direction is given by

$$\phi_{y,\text{effective}}^{h,a} = \phi_y^{h,a} - \theta_{\text{rec}}. \tag{35}$$

5 The edge points of the measurement points are computed by using the Equations (14) to (16) with $n_{m,x}$ and $n_{m,y}$ and adjusted indices. For a point on the left edge we use the adjusted horizontal index $i_l = i - \frac{1}{2}$, for the right edge respectively $i_r = i + \frac{1}{2}$. Analogously we obtain the adjusted vertical index by $j_l = j - \frac{1}{2}$ for the lower and $j_u = j + \frac{1}{2}$ for a point on the upper edge.

6 The offsets of the edge points $x_{o,\text{left}}^{h,a,m}$, $x_{o,\text{right}}^{h,a,m}$, $y_{o,\text{lower}}^{h,a,m}$ and $y_{o,\text{upper}}^{h,a,m}$ (to prevent confusion with the long and short index the indices are written out) for each measurement point are computed by using the Equations (31) and (32).

7 The projected areas $A_{m,o}$ for each measurement point are computed by multiplying the horizontal and the vertical edge lengths and thus given by

$$A_{m,o} = (x_{o,\text{right}}^{h,a,m} - x_{o,\text{left}}^{h,a,m}) \cdot (y_{o,\text{upper}}^{h,a,m} - y_{o,\text{lower}}^{h,a,m}). \tag{36}$$

8 The heat fluxes at the measurement points for every aim point are computed by using Equation (28) with the offsets (x_o, y_o) from **4** and the projected areas $A_{m,o}$ from **7**.

2.5.5 Cylindrical cavity receiver

Projecting the heliostat image onto a cylindrical cavity receiver is analogous to the procedure done for the rectangular receiver in Section 2.5.4 except that we need to project the measurement and aim points onto a plane in front of the receiver first.

1 The Cartesian coordinates of the aim point are computed using the Equations (17) to (19) with $n_{a,x}$ and $n_{a,y}$.

2 With the coordinates $x_{a(i,j)}$, $y_{a(i,j)}$ and $z_{a(i,j)}$ of the aim point and x_h, y_h and z_h of the heliostat it is possible to compute the intersection point (index isp) from the ray at the middle of the heliostat image and the imaginary plane in front of the receiver at $z = 0$:

$$x_{\text{isp},a} = x_h + s \cdot \left(x_{a(i,j)} - x_h\right) \tag{37}$$
$$y_{\text{isp},a} = y_h + s \cdot \left(y_{a(i,j)} - y_h\right) \tag{38}$$
$$z_{\text{isp},a} = z_h + s \cdot \left(z_{a(i,j)} - z_h\right) \tag{39}$$

with $s = -\frac{z_h}{z_{a(i,j)} - z_h}$

3 The Cartesian coordinates of the measurement are computed using the Equations (17) to (19) with $n_{m,x}$ and $n_{m,y}$.

4 The intersection points (with the coordinates $x_{\text{isp},m}$, $y_{\text{isp},m}$ and $z_{\text{isp},m}$) for each measurement point can be computed analogously to **2** by using the coordinates $x_{m(i,j)}$, $y_{m(i,j)}$ and $z_{m(i,j)}$ from **3** instead of $x_{a(i,j)}$, $y_{a(i,j)}$ and $z_{a(i,j)}$.

If it holds that

- $x_{\text{isp},m} < -r$
- $x_{\text{isp},m} > r$
- $y_{\text{isp},m} < 0$
- $y_{\text{isp},m} > h$

the receiver is not going to be hit, thus the intensity hitting that measurement point is zero. The following steps are not necessary for such a measurement point.

5 The distances Δx and Δy between the intersection points of the measurement points and the intersection point of the aim point are trivially computed by

$$\Delta_x = x_{\text{isp},m} - x_{\text{isp},a} \quad \text{and} \tag{40}$$
$$\Delta_y = y_{\text{isp},m} - y_{\text{isp},a}. \tag{41}$$

6 The offsets $x_o^{h,a,m}$ and $y_o^{h,a,m}$ (respectively long or short, depending on the position of the heliostat relative to the aim point) are obtained by using Equation (31) or (32) respectively by using the distance from **5** as x_r or x_l.

7 The edge points of the measurement points are computed by using the Equations (17) to (19) with $n_{m,x}$ and $n_{m,y}$ and adjusted indices. For a point on the left edge we use the adjusted horizontal index $i_l = i + \frac{1}{2}$, for the right edge respectively $i_r = i - \frac{1}{2}$. Analogously we obtain the adjusted vertical index by $j_l = j - \frac{1}{2}$ for the lower and $j_u = j + \frac{1}{2}$ for a point on the upper edge.

8 The intersection points for each edge point for every measurement point are computed analogously to **2** using the coordinates of the edge points from **7**.

9 The offsets of the edge points $x^{h,a,m}_{o,\text{left}}$, $x^{h,a,m}_{o,\text{right}}$, $y^{h,a,m}_{o,\text{lower}}$ and $y^{h,a,m}_{o,\text{upper}}$ (to prevent confusion with the long and short index the indices are written out) are computed by using the Equations (31) and (32).

10 The projected areas $A_{m,o}$ for each measurement point are computed by multiplying the horizontal and the vertical edge lengths and thus given by

$$A_{m,o} = (x^{h,a,m}_{o,\text{right}} - x^{h,a,m}_{o,\text{left}}) \cdot (y^{h,a,m}_{o,\text{upper}} - y^{h,a,m}_{o,\text{lower}}). \tag{42}$$

11 The heat fluxes at the measurement points are computed by using Equation (28) with the offsets (x_o, y_o) from **6** and $A_{m,o}$ from **10**.

2.5.6 Cylindrical external receiver

Projecting the heliostat image onto a cylindrical external receiver is analogous to the procedure done for the cylindrical cavity receiver in Section 2.5.5 except that the projection plane in front of the receiver has to be moved in dependence of the targeted aim point.

1 The coordinates of the aim points are computed using Equations (20) to (22) with $n_{a,x}$ and $n_{a,y}$. They can be described by the angle $\phi_a = \frac{360}{n_{a,x}} \cdot (i-1)$ with i being the horizontal aim point index. The direction of the heliostat $h \in H$ can also be described by an angle ϕ_h, which is given by

$$\phi_h = \begin{cases} 90 - \text{atan}(\frac{x_h}{z_h}) & \text{for } z_h \leq 0 \\ 90 - \text{atan}(\frac{x_h}{z_h}) + 180 & \text{for } z_h > 0. \end{cases} \tag{43}$$

Due to the shape of the solar tower being a circle in the x-z-plane it becomes apparent that an aim point at the receiver surface for that heliostat is only targetable for

$$\phi_a \in (\phi_h - 90, \phi_h + 90). \tag{44}$$

If this is not given, the following steps do not need to be done for that aim point.

2 The planes in front of the receiver at which the offsets are computed are given by the tangent planes of the receiver, touching it at the intended aim points. Thus the intersection points ($x_{\text{isp},a}$,$y_{\text{isp},a}$,$z_{\text{isp},a}$) of the rays hitting the intended aim points with that planes are trivially given, as they are the intended aim points themself.

3 The Cartesian coordinates of the measurement points are computed using Equations (20) to (22) with $n_{m,x}$ and $n_{m,y}$. If for $\phi_m = \frac{360}{n_{m,x}} \cdot (i-1)$ it holds that

$$\phi_m \in (\phi_h - 90, \phi_h + 90) \tag{45}$$

the measurement point can be hit, otherwise the intensity at that measurement point is zero, as the tower is blocking the radiation and the following steps do not need to be done for that measurement point.

4 With the intersection point as the aim points and the offset being known it again is possible to compute the points at which the receiver surface is hit.

The rays are described by the following equations:

$$x = x_h + s \cdot (x_{m(i,j)} - x_h) \tag{46}$$
$$y = y_h + s \cdot (y_{m(i,j)} - y_h) \tag{47}$$
$$z = z_h + s \cdot (z_{m(i,j)} - z_h), \tag{48}$$

where s needs to be determined in a way, that the receiver surface is hit. Note that we now also have to take the offset in z-direction into account.

The receiver surface analogously to the cavity receiver is described by

$$x \in [-r, r] \tag{49}$$
$$y \in [0, h] \tag{50}$$
$$z = \pm\sqrt{r^2 - x^2}. \tag{51}$$

with z now being able to be negative and positive as it describes a whole cylinder.

The tangent planes that connect with the receiver surface at the aim points are given by

$$x = x_{a(i,j)} + t \cdot 0 + u \cdot \sin\left(\frac{360}{n_{a,x}} \cdot (i-1)\right) \tag{52}$$
$$y = y_{a(i,j)} + t \cdot 1 + u \cdot 0 \tag{53}$$
$$z = z_{a(i,j)} + t \cdot 0 - u \cdot \cos\left(\frac{360}{n_{a,x}} \cdot (i-1)\right). \tag{54}$$

The coordinates $x_{\text{isp},m}$, $y_{\text{isp},m}$ and $z_{\text{isp},m}$ of the intersection points from the rays hitting the measurement points with the plane then are obtained by equating the Equations (46), (47) and (48) with (52), (53) and (54), determining s and plugging it into the Equation (46) seq or determining t and u and plugging it into Equation (52) seq. Here we solve for s and obtain

$$s = \frac{z_{a(i,j)} - z_h - \frac{x_h - x_{a(i,j)}}{\tan(\frac{360}{n_{a,x}} \cdot (i-1))}}{z_{m(i,j)} - z_h + \frac{x_{m(i,j)} - x_h}{\tan(\frac{360}{n_{a,x}} \cdot (i-1))}}. \tag{55}$$

For $\frac{360}{n_{a,x}} \cdot (i-1) = 0$ or $\frac{360}{n_{a,x}} \cdot (i-1) = 180$, we use

$$s = \frac{x_{a(i,j)} - x_h}{x_{m(i,j)} - x_h}, \tag{56}$$

which is the result of equating the Equations (46) and (52) while eliminating the sinus term as it is zero.

5 The distances Δx and Δy between the intersection points of the measurement points and the aim point are computed analogously to the approaches for the other receiver types with the difference, that we have to consider the x and z components. To get the distance in the x-z-plane we use the Euclidean norm.

$$\Delta_x = \sqrt{(x_{\text{isp},m} - x_{\text{isp},a})^2 + (z_{\text{isp},m} - z_{\text{isp},a})^2} \tag{57}$$

$$\Delta_y = y_{\text{isp},m} - y_{\text{isp},a} \tag{58}$$

6,7 These steps are analogous to the cavity receiver in Section 2.5.5.

8 This step also in analogous to the cavity receiver in Section 2.5.5, except that we have to use the Equations (46) to (48) with (55) or respectively (56).

9-11 These steps are also analogous to the cavity receiver in Section 2.5.5.

2.5.7 Refinement

After computing the intensity for each measurement point at the receiver for every heliostat and every aim point, the heliostat images are obtained successfully. When storing the results, these computations only need to be done once and can be done before running the optimization. For this reason the amount of time needed for the computation is negligible, which makes it possible to make the computation even more accurate by using refinement.

For the refinement process we choose the refinement factors ref_x and ref_y in the x- and y- direction. We then define a new set of measurement points M_{ref} containing the increased number of measurement point, thus a finer measurement point grid

$$M_{\text{ref}} = \{(i,j) : i \in \{1, ..., n_{m,x} \cdot \text{ref}_x\}, j \in \{1, ..., n_{m,y} \cdot \text{ref}_y\}\}. \tag{59}$$

We then compute the heat flux intensity at every measurement point $m \in M_{\text{ref}}$ for every $a \in A$ and every $h \in H$. Using a finer measurement point grid corresponds to using a higher number of points for the two-dimensional mid point rule from Equation (24) or respectively (28).

After we computed the heliostat images with the heat fluxes $Q_{x,y}^{h,a,\text{ref}}$ using M_{ref} we sum them up to obtain the heliostat images as defined for the set of measurement points M

$$Q_{x,y}^{h,a} = \sum_{i=0}^{\text{ref}_x-1} \sum_{j=0}^{\text{ref}_y-1} Q_{x+i,y+j}^{h,a,\text{ref}}. \tag{60}$$

2.6 Results

The relative heat flux distributions at a rectangular external receiver with the resolution $(n_{m,x}, n_{m,y}) = (20, 20)$ are shown in the Figures 14 to 17. Each heliostat has the same vertical distance to the aim point, but the horizontal distances differ. The axes were chosen as defined in Figure 7. For Figure 17 the aim point was set to the top left corner.

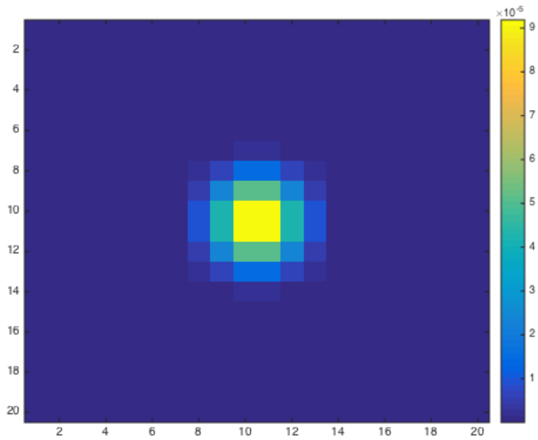

Figure 14: $x = 0, y = 0, z = 200$

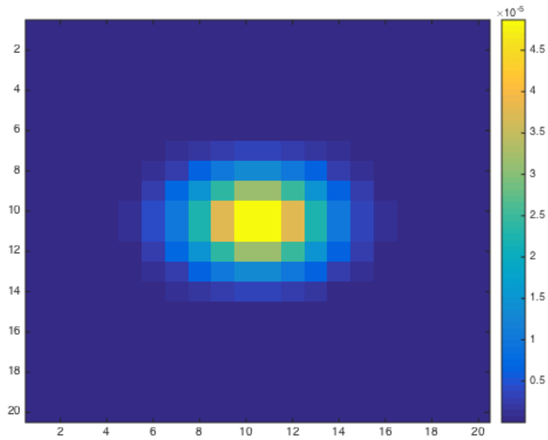

Figure 15: $x = -220, y = 0, z = 200$

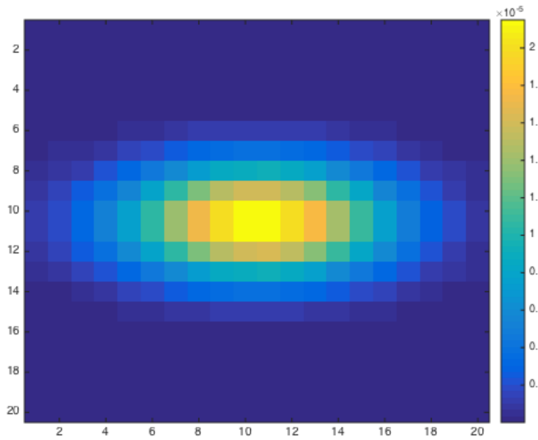

Figure 16: $x = -440, y = 0, z = 200$

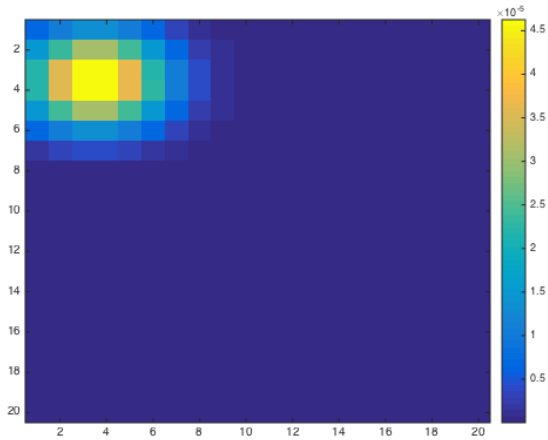

Figure 17: $x = -220, y = 0, z = 200$

The following receiver parameters were used:

h_{tower}	120m
h_{top}	0m
w_{rec}	20m
h_{rec}	20m
θ_{rec}	0°

3 Deterministic aiming strategy

In Section 2 we computed the heliostat images $Q^{h,a}$ as matrices for every heliostat and every aim point. Our objective is to find the optimal choice of aim points at a fixed time in a way that the maximum available heat flux is transferred to the receiver while not violating any safety constraints.

This optimization model describes the deterministic aiming strategy as an ILP. We assume a scenario in which uncertainties as inaccurate tracking are neglected. The optimization model is highly based on [5] as we use this model and extend it to also take gradient limits into account.

At first we look at the definitions needed, before we go into detail with the optimization model by deriving the objective function and constraints.

3.1 Definitions

3.1.1 Heliostats

The heliostats (introduced in Section 2.3) are focussing the irradiation of the sun onto one of the aim points at the receiver surface. The set containing them is defined by Equation (3) as

$$H = \{1, ..., n_h\},$$

where n_h is the number of heliostats.

3.1.2 Measurement points

The measurement points (introduced in 2.4.3) are the points at the receiver surface at which the simulated heat fluxes hitting the subarea around the respective measurement point are summed up. The set containing them is defined by Equation (12) as

$$M = \{(i, j) : i \in \{1, ..., n_{m,x}\}, j \in \{1, ..., n_{m,y}\}\},$$

where $n_{m,x}$ and $n_{m,y}$ are the number of measurement points in the x and y dimension.

3.1.3 Aim points

The aim points (introduced in 2.4.4) are the points at the receiver surface, that can be targeted by heliostats. The set containing them is defined by Equation (13) as

$$A = \{(i, j) : i \in \{1, ..., n_{a,x}\}, j \in \{1, ..., n_{a,y}\}\},$$

where $n_{a,x}$ and $n_{a,y}$ are the number of aim points in the x and y dimension.

3.1.4 Decision variables

The decision variables $x^{h,a}$ determine if the heliostat $h \in H$ targets the aim point $a \in A$. A heliostat only can or cannot target an aim point, distributions of the heat flux between two or more aim points are forbidden; thus the decision variables are binary variables, i.e.

$$x^{h,a} \in \{0, 1\} \quad \forall\, h \in H \quad \forall\, a \in A. \tag{61}$$

If heliostat h targets aim point a then $x^{h,a} = 1$ otherwise it is 0.

3.1.5 Local receiver heat flux

The local heat flux Q_m^{receiver} at the receiver surface, which hits the subarea around the measurement point $m \in M$, is obtained by summing up the heat fluxes of the images of every heliostat $Q_{h,a}$ at the measurement point m with respect to the aim point they are targeting:

$$Q_m^{\text{receiver}} = \sum_{h \in H} \sum_{a \in A} Q_m^{h,a} \cdot x^{h,a}. \tag{62}$$

3.2 Objective function

Our objective is to transfer the maximum possible heat flux to the receiver. This means, we want to maximize the total heat flux hitting the receiver Q_{total}, which is the sum of the heat fluxes of every measurement point. Following from this, the objective function is given by

$$\max Q^{\text{total}} = \max \sum_{m \in M} Q_m^{\text{receiver}}. \tag{63}$$

3.3 Constraints

3.3.1 Maximum one aim point per heliostat

Each heliostat can or cannot target an aim point, but the maximum number of aim points targetable per heliostat is one. The reason for this is, that all of the reflected irradiation of a heliostat is sent towards the targeted aim point, thus that there is no irradiation left, which could be reflected towards another aim point.

For the mathematical formulation of the constraint this means, that all of the decision variables of one heliostat have to be smaller or equal to one when summed up:

$$\sum_{a \in A} x^{h,a} \leq 1 \quad \forall h \in H \tag{64}$$

We allow the sum to be smaller than one – we are summing up binary variables thus it is zero in that case – as it is also possible for a heliostat to target no aim point at all.

3.3.2 Upper heat flux limit

Each receiver has an upper limit for the heat flux hitting it, because the material it is made of can only withstand a certain maximum temperature. As mentioned in Section 2.4.2 we assume the maximum heat flux values for the receiver to be given as a $n_{m,x} \times n_{m,y}$ matrix $Q^{\max}$ determined by a thermodynamical simulation.

When constraining the maximum heat fluxes by using a constant maximum heat flux density, e.g. given in $\frac{\text{kW}}{\text{m}^2}$, it is important to note, that this intensity has to be converted into the maximum intensity at the subarea around each measurement point by multiplying the given value by the size of the area that surrounds the respective measurement point.

When doing the optimization we have to make sure, that these values are not exceeded at any measurement point:

$$Q_m^{\text{receiver}} \leq Q_m^{\max} \quad \forall m \in M \tag{65}$$

We do not introduce a lower bound for the heat flux, because this would be an artificial constraint that is not found for receivers in operating power plants. A receiver is not going to be damaged, when a certain heat flux value is undershot. However it may be damaged when the difference between the heat fluxes at two adjacent measurement points is too high, thus we consider this effect in Section 3.3.3 by constraining the heat flux gradient.

3.3.3 Heat flux gradient limit

Additionally to the maximum heat flux, the receiver material has a maximum heat flux gradient it can withstand. We measure that gradient vertically and horizontally.

Usually receivers consist of several plates being arranged next to each other in a vertical or horizontal fashion, which means that the gradients in one direction can be neglected. If the plates are arranged horizontally for example, the horizontal temperature gradients can be neglected, because the plates are not connected in this direction and thus only transfer heat via convection and radiation, but not conduction, which makes the heat transfer much weaker and hence neglectable.

As for the heat flux limit we assume that the heat flux gradient limit is given. For the horizontal gradients we need a $(n_{m,x} - 1) \times n_{m,y}$ matrix $G^{\text{max,horizontal}}$, for the vertical gradients a $n_{m,x} \times (n_{m,y} - 1)$ matrix $G^{\text{max,vertical}}$ containing the maximum values for the gradients in the corresponding directions.

An easy way to define the gradient between two measurement points is

$$\frac{|Q_m^{\text{receiver}} - Q_{m-1}^{\text{receiver}}|}{d}, \tag{66}$$

where d is the distance between the measurement points. In the following we neglect d and assume it to be included in the given heat flux gradient limits $G^{\text{max,horizontal}}$ and $G^{\text{max,vertical}}$.

When constraining the maximum heat flux gradients by using a constant gradient limit e.g. given in $\frac{\text{kW}}{\text{m}}$, we need to scale the gradient limits analogously to the maximum heat flux limits as done in Section 3.3.2 to obtain the maximum allowed heat flux difference between two measurement points. This is done my multiplying the given gradient limit with the distance between the considered measurement points in the respective direction.

For the horizontal gradients we obtain the constraints

$$|Q_{i,j}^{\text{receiver}} - Q_{i-1,j}^{\text{receiver}}| \leq G_{i-1,j}^{\text{max,horizontal}} \tag{67}$$

$\forall\, i \in \{2, ..., n_{m,x}\} \quad \forall\, j \in \{1, ..., n_{m,y}\}$.

For the vertical gradients we obtain the constraints

$$|Q_{i,j}^{\text{receiver}} - Q_{i,j-1}^{\text{receiver}}| \leq G_{i,j-1}^{\text{max,vertical}} \tag{68}$$

$\forall i \in \{1, ..., n_{m,x}\} \quad \forall\, j \in \{2, ..., n_{m,y}\}$.

As we are formulating the optimization problem as an integer linear program we have to linearize the absolute value. This can be done by constraining the differences of the heat flux values at the measurement points in each direction. A negative difference is trivially smaller than a positive upper bound and a positive difference is constrained as before for the absolute value.

For the horizontal gradients we obtain the linearized constraints

$$Q_{i,j}^{\text{receiver}} - Q_{i-1,j}^{\text{receiver}} \leq G_{i-1,j}^{\text{max,horizontal}} \tag{69}$$

$$Q_{i-1,j}^{\text{receiver}} - Q_{i,j}^{\text{receiver}} \leq G_{i-1,j}^{\text{max,horizontal}} \tag{70}$$

$\forall\, i \in \{2, ..., n_{m,x}\} \ \ \forall\, j \in \{1, ..., n_{m,y}\}$.

For the vertical gradients we obtain the linearized constraints

$$Q_{i,j}^{\text{receiver}} - Q_{i,j-1}^{\text{receiver}} \leq G_{i,j-1}^{\text{max,vertical}} \tag{71}$$
$$Q_{i,j-1}^{\text{receiver}} - Q_{i,j}^{\text{receiver}} \leq G_{i,j-1}^{\text{max,vertical}} \tag{72}$$

$\forall i \in \{1, ..., n_{m,x}\} \ \ \forall\, j \in \{2, ..., n_{m,y}\}$.

3.4 Summarized optimization model

- **Definition:**

$$Q_m^{\text{receiver}} = \sum_{h \in H} \sum_{a \in A} Q_m^{h,a} \cdot x^{h,a}.$$

- **Objective function:**

$$\max Q^{\text{total}} = \max \sum_{m \in M} Q_m^{\text{receiver}}$$

- **Decision variables:**

$$x^{h,a} \in \{0, 1\} \ \ \forall\, h \in H \ \ \forall\, a \in A$$

- **First constraint:**

$$\sum_{a \in A} x^{h,a} \leq 1 \ \ \forall\, h \in H$$

- **Second constraint:**

$$Q_m^{\text{receiver}} \leq Q_m^{\text{max}} \ \ \forall\, m \in M$$

- **Third constraint:**

$$Q_{i,j}^{\text{receiver}} - Q_{i-1,j}^{\text{receiver}} \leq G_{i-1,j}^{\text{max,horizontal}}$$
$$Q_{i-1,j}^{\text{receiver}} - Q_{i,j}^{\text{receiver}} \leq G_{i-1,j}^{\text{max,horizontal}}$$

$\forall\, i \in \{2, ..., n_{m,x}\} \ \ \forall\, j \in \{1, ..., n_{m,y}\}$

$$Q_{i,j}^{\text{receiver}} - Q_{i,j-1}^{\text{receiver}} \leq G_{i,j-1}^{\text{max,vertical}}$$
$$Q_{i,j-1}^{\text{receiver}} - Q_{i,j}^{\text{receiver}} \leq G_{i,j-1}^{\text{max,vertical}}$$

$\forall\, i \in \{1, ..., n_{m,x}\} \ \ \forall\, j \in \{2, ..., n_{m,y}\}$

3.5 Heat shield

As mentioned in Section 2.4, a solar tower usually is equipped with a heat shield, that protects it from radiation missing the receiver surface. Radiation hitting the heat shield is not transferred to a heat carrying medium thus that radiation is not used to generate electrical energy, which results in being undesirable.

Even though we try to avoid radiation missing the receiver, we have to make sure that maximum temperatures and maximum temperature gradients at the heat shield are not exceeded.

For taking the heat shield into account we can define the additional set $M_{\text{heatshield}}$ containing the measurement points discretizing the heat shield. We do not have to define an additional set for the aim points, as targeting the heat shield is undesirable.

We still use the smaller set M containing the measurement points at the receiver surface for the objective function, hence we only summarize the parts of the heliostat images hitting the receiver surface and neglect the parts hitting the heat shield as those do not lead to the transfer of thermal energy to the heat carrying medium.

For the maximum heat flux constraints we have to make sure, that they hold for the measurement points at the heat shield additionally to the measurement points at the receiver surface thus we introduce additional constraints $\forall\, m \in M_{\text{heatshield}}$ additionally to the known constraints $\forall\, m \in M$.

For the heat flux gradients we have to introduce additional constraints between the receiver and the heat shield if these components are directly physically connected and heat transfer between both components shall be considered. Additionally we have to introduce constraints if we want to consider gradients between heat shield points in the respective directions.

If both of the above cases hold true we introduce additional constraints $\forall\, m \in M_{\text{heatshield}}$. If only one of the above cases holds true we introduce additional constraints for the respective subset of $M_{\text{heatshield}}$. If we neither consider gradients between the receiver and the heat shield nor between the heat shield points we do not have to introduce new constraints.

3.6 Clouds

As described in Section 2.2, CSP plants can only use direct radiation. This type of radiation can be absorbed or reflected by clouds, which means that a heliostat image is (partly) zero, if a cloud is (partly) positioned between the sun and the heliostat.

When dropping the assumption of a cloudless sky and assuming that the positions of the clouds thus that the shaded heliostats are known, we can adjust our optimization model and take clouds into account. In the following we assume that a heliostat either is shaded completely or not shaded at all.

With the set of shaded heliostats

$$H_{\text{shaded}} = \{h \in H | \, h \text{ is shaded}\}, \tag{73}$$

we can define a new set of heliostats

$$H_{\text{hit}} = H \backslash H_{\text{shaded}}, \tag{74}$$

which describes the set of heliostats, whose images are not zero due to cloud shading. We then can use the set H_{hit} instead of our default set H for the optimization model, effectively reducing the size of the problem as we do not have to consider $|H_{\text{shaded}}| \cdot |A|$ decision variables.

3.7 Obtaining a specified receiver heat flux distribution

In reality it usually is not only mandatory to satisfy the constraints that prevent damaging of the receiver but also to obtain a certain heat flux distribution.

On the one hand the task of the receiver is, to absorb the thermal energy, that is projected onto it by the heliostats. On the other hand this energy has to be transferred to the heat carrying medium. If for instance all of the radiation is concentrated onto a small area at the receiver – for now we assume without violating a constraint – it still might not be an optimal solution, because the heat carrying medium will not be heated anywhere except at that small area.

For this reason there exist desired receiver heat flux distributions that can be computed by doing thermodynamical simulations. Sometimes these heat flux distributions may not only be desired but form actual constraints, because of the material at certain receiver areas not being able to withstand certain temperatures. In these cases we speak of allowed flux density (AFD). Such an allowed flux density given in Figure 18.

If this kind of distribution is given, we can just use it as a regular constraint as described in Section 3.3.2. If, however, the heat flux distribution is desired but not mandatory, we cannot just use it as a constraint, because we might miss out on optimization potential by not using the total of the available thermal energy.

In these cases we can convert a given desired absolute heat flux distribution into a relative one. If the resolution of the grid used in the thermodynamical simulation does not fit our measurement points grid by either being to fine or too rough, we can additionally resolve the given distribution to fit our measurement point grid. The results for measurement point resolutions given by $(n_{m,x}, n_{m,y})_a = (6, 4)$ and $(n_{m,x}, n_{m,y})_b = (12, 8)$

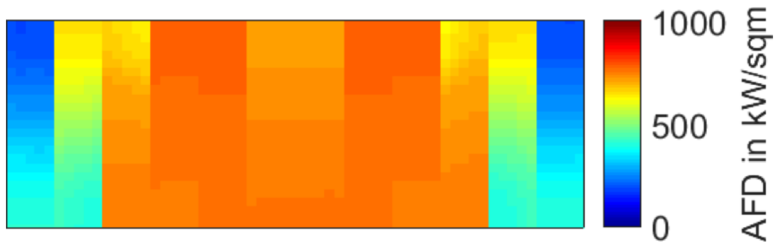

Figure 18: The desired heat flux profile for a receiver as allowed flux density (AFD) given as absolute heat flux density. It is visible, that the tubes containing the heat carrying medium enter the inner of the receiver area from the upper corners and are arranged in serpentines leaving the inner of the receiver area around the center.

are shown in the Figures 19a and 19b.

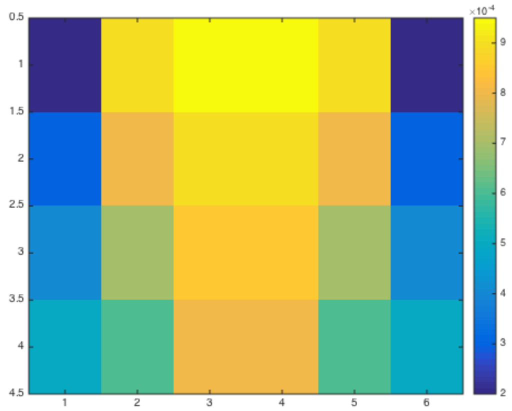

(a) Receiver resolution: 6×4

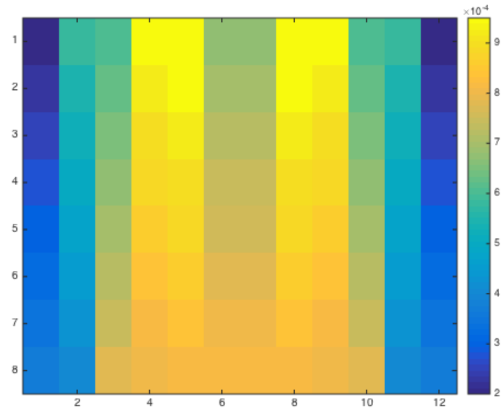

(b) Receiver resolution: 12×8.

Figure 19: The desired heat flux profiles for a receiver given as relative heat flux density.

With the relative distribution available we can scale it with a chosen maximum heat flux intensity. The scaling intensity has to be smaller or equal to the the actual constraint determined by the receiver material, but technically has no lower bound. By experimenting one can determine the optimal heat flux intensity. If the receiver distribution deviates too much from the desired distribution, the maximum heat flux intensity is too large. Ff some heliostats do not target an aim point at all, it is too small.

After the scaling heat flux intensity is determined, we can use the relative distribution multiplied with the scaling factor for constraining the maximum heat flux.

4 Robust aiming strategy

In Section 3 we derived an optimization model for an optimal aiming strategy under deterministic circumstances as an ILP In this section we extend that optimization model and take the tracking errors of the heliostats into account, obtaining an MILP.

As described in Section 2.3 tracking errors can be caused by various effects and cause the heliostat to target another point than intended. As the whole heliostat image is moved to a different location, violations of the heat flux or heat flux gradient limits at the receiver can occur. The effects of tracking errors on different heliostats in respect to the total heat flux distribution do not cancel each other out; for this reason we have to consider the tracking errors as an uncertainty and must not consider it by simply enlarging the Gaussian distribution representing a heliostat image. More details to tracking errors and their non-Gaussian behaviour can be found in [11].

To model tracking errors we use a robust optimization approach called Gamma robustness [8], i.e. we allow a previously determined number of heliostats Γ to deviate. With the Gamma robustness approach it is possible to specify different Γ values for each considered constraint to specify different requirements of robustness. For the sake of simplicity however, we assume Γ to be constant.

If a heliostat $h \in H$ deviates from its intended aim point, its image can be moved. We assume the usual case, that the heliostat is tracked biaxially, thus the horizontal and the vertical tracking error $\sigma_{\text{tracking,hor}}$ and $\sigma_{\text{tracking,ver}}$ determine the maximum deviation distances $d^{\max,h}_{\text{dev,hor}}$ and $d^{\max,h}_{\text{dev,ver}}$ the heliostat image can be moved in the respective directions. Depending on the location the heliostat actually targets we then adjust the heat flux value at every measurement point.

In the following we extend the optimization model from Section 3, meaning we use the definitions, objective function and constraints from Section 3 and extend them to take the tracking errors into account. For the sake of simplicity, however, we neglect the heat flux gradients at the receiver.

4.1 Definitions

4.1.1 Additional decision variables

Additionally to the decision variables $x^{h,a}$ indicating if heliostat $h \in H$ targets aim point $a \in A$, we introduce the decision variables $\hat{x}^h_m$ indicating if heliostat h deviates from any aim point it targets towards the measurement point $m \in M$. A heliostat only can or cannot deviate from an originally intented aim point, thus these decision variables are binary as well, i.e.

$$\hat{x}^h_m \in \{0, 1\} \quad \forall h \in H \quad \forall m \in M. \tag{75}$$

If heliostat h deviates towards measurement point m then $\hat{x}^h_m = 1$ otherwise it is 0.

4.1.2 Adjusted local receiver heat flux

We adjust the local receiver heat flux Q_m^{receiver} by introducing the additional local heat flux $\hat{Q}_m^{h,a}$. It represents the worst case difference in the heat flux at the measurement point $m \in M$, when heliostat $h \in H$ does not directly hit the intended aim point $a \in A$ due to tracking errors.

$\hat{Q}_m^{h,a}$ is defined in a way that the worst case that can possibly occur is still considered in its formulation: When trying to prevent that a heat flux limit is exceeded, the worst case possible is, that a heliostat deviates the largest possible distance from the original aim point a towards the measurement point m, because this results in the largest possible difference between the initial heat flux value without deviation and the actual heat flux value obtained by considering deviation hitting the subarea around the measurement point m.

For this reason we define the worst case of the additional local heat flux $\hat{Q}_m^{h,a}$ by using the worst thus highest heat flux intensity $Q_{\text{worst},m}^{h,a}$ at m when h initially aimed at a, as

$$\hat{Q}_m^{h,a} = Q_{\text{worst},m}^{h,a} - Q_m^{h,a}. \tag{76}$$

$Q_{\text{worst},m}^{h,a}$ in turn is obtained by either bilinearily interpolating the heat flux intensity hitting the subarea around m by using the heat flux values at m of the heliostat images which aim points surround the worst case aim point or by precomputing the heat flux value when h aims at the worst case aim point directly.

The adjusted local receiver heat flux $\hat{Q}_m^{\text{receiver}}$ then can be written for a possible but fixed choice of $\hat{x}_m^h$ as a sum of the known local receiver heat flux from Section 3 and an additional term to take the possible deviation of the heliostats into account:

$$\hat{Q}_m^{\text{receiver}} = \sum_{h \in H} \sum_{a \in A} Q_m^{h,a} \cdot x^{h,a} + \sum_{h \in H} \sum_{a \in A} \hat{Q}_m^{h,a} \cdot x^{h,a} \cdot \hat{x}_m^h. \tag{77}$$

4.1.3 Worst case aim point

The worst case aim point is the point that is closest to the measurement point $m \in M$ while deviating the maximum possible distances $d_{\text{dev,hor}}^{\text{max},h}$ and $d_{\text{dev,ver}}^{\text{max},h}$ from the original aim point $a \in A$ for the heliostat $h \in H$. We only derive the equations for the horizontal deviation distance. They also hold for the vertical deviation distance analogously.

If $d_{\text{dev,hor}}^{\text{max},h}$ exceeds the horizontal distance $d_{\text{hor}}^{a,m}$ between a and m, the worst case horizontal coordinate is the horizontal coordinate m_{hor} of measurement point m ifself, as a focus point of a heliostat image through deviation beyond m would reduce the heat flux hitting m and thus not be the worst possible point with respect to m.

The horizontal coordinate represents the x-coordinate for a rectangular receiver and the x- and z- coordinate for cylindrical receiver types, because for these the x- and z-coordinates depend on each other. Analogously the vertical coordinate represents the y- and z-coordinate for tilted rectangular and only the y coordinate for cylindrical receiver types.

With the coordinates m_{hor} and a_{hor} of m and a as well as the distances $d_{\text{hor}}^{a,m}$ and $d_{\text{dev,hor}}^{\max,h}$ being known, we can compute the horizontal coordinate $w_{\text{hor},m}^{h,a}$ of the worst case aim point $w_m^{h,a}$ as

$$w_{\text{hor},m}^{h,a} = \begin{cases} m_{\text{hor}}, & d_{\text{dev,hor}}^{\max,h} \geq d_{\text{hor}}^{a,m} \\ a_{\text{hor}} + \frac{d_{\text{dev,hor}}^{\max,h}}{d_{\text{hor}}^{a,m}} \cdot (m_{\text{hor}} - a_{\text{hor}}), & \text{otherwise.} \end{cases} \tag{78}$$

For cylindrical receiver types we do not use the coordinates of the measurement and aim point on the receiver surface m_{hor} and a_{hor}, but the coordinates of the projection of these points onto a plane in front of the receiver as done in the Sections 2.5.5 and 2.5.6. The worst case point $w_m^{h,a}$ then is obtained on that plane as well. We do not have to project it back onto the receiver surface, as the computation of the heat fluxes with the respective worst case aim point is done on that plane anyway.

The horizontal maximum possible deviation distance $d_{\text{dev,hor}}^{\max,h}$ is analogously obtained by projecting the horizontal unprojected maximum deviation distance $\hat{d}_{\text{dev,hor}}^{\max}$ onto a plane in front of the receiver. The worst case aim point then can be determined by computing the worst case aim point on the plane with the equations above and projecting it onto the receiver surface.

The undistorted maximum deviation distance depends on the distance between heliostat h and aim point a in the x-z-plane $\hat{d}_x^{h,a}$ as introduced in Section 2.5.3 and the horizontal tracking error:

$$\hat{d}_{\text{dev,hor}}^{\max,h} = \tan(\sigma_{\text{tracking,hor}}) \cdot \hat{d}_x^{h,a}. \tag{79}$$

With that knowledge, we can compute the maximum possible horizontal deviation distance $d_{\text{dev,hor}}^{\max,h}$ by using the inverse functions of the Equations (31) and (32). With $\phi_x^{h,a}$ being the incident angle in x-direction as defined in Section 2.5.3, we can determine the maximum possible horizontal deviation distance for deviation towards a point positioned on the heliostat's side of the aim point a to

$$d_{\text{dev,hor}}^{\max,h} = \frac{\hat{d}_x^{h,a} \cdot \hat{d}_{\text{dev,hor}}^{\max}}{\hat{d}_x^{h,a} \cdot \cos(\phi_x^{h,a}) + \hat{d}_{\text{dev,hor}}^{\max} \cdot \sin(\phi_x^{h,a})} \tag{80}$$

and for deviation towards a point positioned on the opposite site of the aim point a to

$$d_{\text{dev,hor}}^{\max,h} = \frac{\hat{d}_x^{h,a} \cdot \hat{d}_{\text{dev,hor}}^{\max}}{\hat{d}_x^{h,a} \cdot \cos(\phi_x^{h,a}) - \hat{d}_{\text{dev,hor}}^{\max} \cdot \sin(\phi_x^{h,a})}. \tag{81}$$

As the heliostat images, the worst case aim points for each heliostat and measurement point can be precomputed.

4.1.4 Worst case local heat flux

As mentioned in Section 4.1.2 the heat flux $Q^{h,a}_{\text{worst},m}$ at the measurement point $m \in M$ for the worst case when the heliostat $h \in H$ targets the aim point $a \in A$ can be computed by using either bilinear interpolation or precomputation of the heat flux at m. We are going to look at these approaches now.

Bilinear interpolation When the coordinates $(w^{h,a}_{\text{hor},m}, w^{h,a}_{\text{ver},m})$ of the worst case aim point $w^{h,a}_m$ are known, we can determine the coordinates of the aim points surrounding it. For the sake of legibility we neglect the indices that show, that these aim points depend on h and m, as they surround a worst case aim point chosen in respect to m for the heliostat h. We choose their left and right horizontal coordinates $a_{\text{hor,l}}$ and $a_{\text{hor,r}}$ and their lower and upper vertical coordinates $a_{\text{ver,l}}$ and $a_{\text{ver,u}}$ in a way that

$$w^{h,a}_{\text{hor},m} = [a_{\text{hor,l}}, a_{\text{hor,r}}) \tag{82}$$

$$w^{h,a}_{\text{ver},m} = [a_{\text{ver,l}}, a_{\text{ver,u}}). \tag{83}$$

For cylindrical receiver types we project the aim points onto a plane in front of the receiver as done in the Sections 2.5.5 and 2.5.6 and then choose the coordinates of the projected points accordingly. The surrounding aim points or respectively their projections then are given by $a_1 = (a_{\text{hor,l}}, a_{\text{ver,l}})$, $a_2 = (a_{\text{hor,l}}, a_{\text{ver,u}})$, $a_3 = (a_{\text{hor,r}}, a_{\text{ver,l}})$ and $a_4 = (a_{\text{hor,r}}, a_{\text{ver,u}})$.

As the heat fluxes $Q^{h,a}_m$ with $a = a_1$ to $a = a_4$ at these aim points are known, we can approximate $Q^{h,a}_{\text{worst},m}$ by using bilinear interpolation, which results in

$$\begin{aligned}
Q^{h,a}_{\text{worst},m} \approx\ & Q^{h,a_1}_m \cdot \Big(1 - \frac{w^{h,a}_{\text{hor},m}}{a_{\text{hor,r}} - a_{\text{hor,l}}}\Big(1 - \frac{w^{h,a}_{\text{ver},m}}{a_{\text{ver,u}} - a_{\text{ver,l}}}\Big) - \frac{w^{h,a}_{\text{ver},m}}{a_{\text{ver,u}} - a_{\text{ver,l}}}\Big) \\
&+ Q^{h,a_2}_m \cdot \Big(\frac{w^{h,a}_{\text{hor},m}}{a_{\text{hor,r}} - a_{\text{hor,l}}}\Big(1 - \frac{w^{h,a}_{\text{ver},m}}{a_{\text{ver,u}} - a_{\text{ver,l}}}\Big)\Big) \\
&+ Q^{h,a_3}_m \cdot \Big(\frac{w^{h,a}_{\text{ver},m}}{a_{\text{ver,u}} - a_{\text{ver,l}}}\Big(1 - \frac{w^{h,a}_{\text{hor},m}}{a_{\text{hor,r}} - a_{\text{hor,l}}}\Big)\Big) \\
&+ Q^{h,a_4}_m \cdot \Big(\frac{w^{h,a}_{\text{hor},m}}{a_{\text{hor,r}} - a_{\text{hor,l}}}\frac{w^{h,a}_{\text{ver},m}}{a_{\text{ver,u}} - a_{\text{ver,l}}}\Big).
\end{aligned}$$

Precomputation For precomputing $Q^{h,a}_{\text{worst},m}$ we just have to determine the heat flux at m when h targets the worst case aim point $w^{h,a}_m$. The coordinates of $w^{h,a}_m$ are computed by using Equation (78) and now represent the coordinates of the adjusted aim point. As the coordinates of m are known, the local heat flux then can be computed by using Equation (28) as

$$Q^{h,a}_{\text{worst},m} = Q^{h,w}_{x,y}. \tag{84}$$

4.1.5 Interpolation versus precomputation

As precomputing and storing the worst case heat fluxes is an exact computation method, it is preferable over interpolating heat fluxes. Additionally it can be done during the offline runtime of the optical model, which means that it does not increase the runtime of the optimization model, making it beneficial if computations in real time are desired.

However, especially for large solar tower power plants memory storage might not be available, hence it might not be possible to store both the worst case heat fluxes or respectively the additional heat fluxes and the heliostat images.

This problem can be further increased if a fine discretization in time is required. In this case numerous versions of heliostat images have to be computed for different time steps and sun positions. In these cases interpolation is preferable.

In the Figures 20a and 20b the relative errors between the exact computation and the interpolation of the worst case heat fluxes for a rectangular external receiver are shown. The heat flux values at the corners are used to interpolate the intensities at the considered measurement point for worst case aim points positioned between them. For this reason the relative errors are zero at the corners as the interpolation is exact there.

The order of magnitude of the relative error between the interpolation and the exact computation of the worst case heat fluxes is between 0 and 10^{-4} for both a heliostat without and a heliostat with a horizontal offset to the receiver. This confirms, that it is possible to use interpolation for computing the worst case heat fluxes without introducing large errors.

4.2 Objective function

As in Section 3 the objective function is given by

$$\max Q^{\text{total}} = \max \sum_{m \in M} Q_m^{\text{receiver}}. \tag{85}$$

Note that we do not use $\hat{Q}_m^{\text{receiver}}$ in the objective function, but only as a constraint for the upper heat flux.

$\hat{Q}_m^{\text{receiver}}$ can only be computed for a possible but fixed choice of $\hat{x}_m^h$, which have to be chosen in the way that the maximum of the additional local heat flux for a measurement point is found. Hence summing up $\hat{Q}_m^{\text{receiver}}$ would not only not be the objective we are optimizing for, but also be incorrect, because we would be summing up the worst cases for each measurement point, which cannot occur simultaneously.

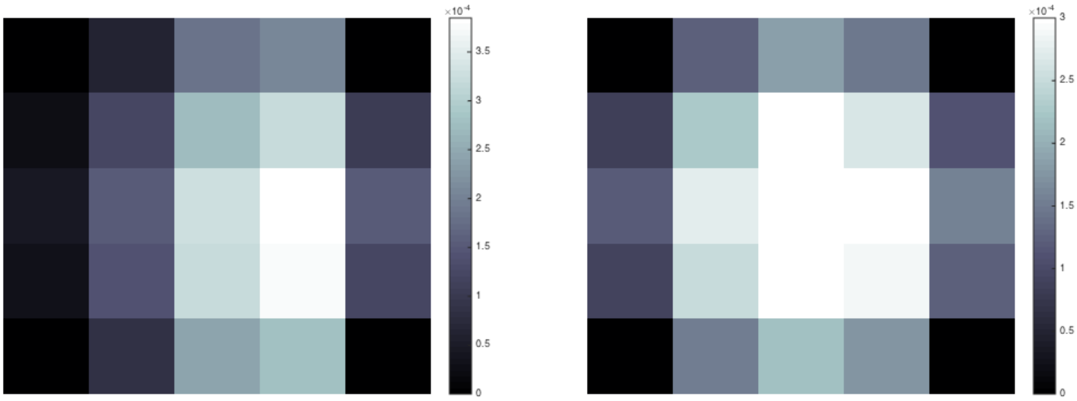

(a) No horizontal offset for a heliostat positioned 200m away from the receiver.

(b) 300m horizontal offset for a heliostat positioned 200m away from the receiver.

Figure 20: Relative errors between the exact computation and the interpolation of the worst cases heat fluxes.

4.3 Constraints

4.3.1 Maximum number of deviating heliostats

When allowing each heliostat to deviate the maximum possible distance, we are going to obtain unrealistic results, as in reality neither every heliostat is going to deviate nor the deviating heliostats are going to miss the intended aim point by the maximum distance.

For this reason we define the number Γ of deviating heliostats, for which holds that

$$0 \leq \Gamma \leq |H|. \tag{86}$$

Γ can be determined by running the aiming strategy for a given plant setup with different parameters several times and comparing the results. The smaller Γ is, the better but potentially unsafer is the obtained solution going to be.

For a chosen Γ, we can formulate the constraint for the number of deviating heliostats regarding each measurement point m as

$$\sum_{h \in H} \hat{x}_m^h \leq \Gamma \quad \forall m \in M. \tag{87}$$

4.3.2 Heat flux limit

Analogously to Section 3 we introduce an upper heat flux limit by constraining the heat flux at every measurement point. However, we cannot simply replace Q_m^{receiver} by

$\hat{Q}_m^{\text{receiver}}$ in Equation (65), as the latter describes the adjusted local receiver heat flux for a possible but fixed choice of $\hat{x}_m^h$ and we are looking to find the worst case.

This does not only mean, that we have to consider the maximum deviation distance $d_{\text{deviation}}^{\max}$, when computing $\hat{Q}_m^{h,a}$ and hence $\hat{Q}_m^{\text{receiver}}$, but also that we have to make sure that all possible combinations of the adjusted local heat flux $\hat{Q}_m^{\text{receiver}}$ are feasible. Thus we need to determine the maximum of $\hat{Q}_m^{\text{receiver}}$, i.e. the maximum of $\hat{Q}_m^{h,a} \cdot x^{h,a} \cdot \hat{x}_m^h$ from Equation (77), which leads to a nested optimization model for the respective measurement point m given by:

- **Objective function:** maximize the possible additional local heat flux

$$\hat{\alpha}_m(x^{h,a}) = \max \sum_{h \in H} \sum_{a \in A} \hat{Q}_m^{h,a} \cdot x^{h,a} \cdot \hat{x}_m^h$$

- **Decision variables:** every heliostat only can or cannot deviate

$$\hat{x}_m^h \in \{0, 1\} \quad \forall h \in H$$

- **Constraint:** maximum Γ deviating heliostats

$$\sum_{h \in H} \hat{x}_m^h \leq \Gamma$$

The total heat flux limit constraint then is given by

$$\sum_{h \in H} \sum_{a \in A} Q_m^{h,a} \cdot x^{h,a} + \hat{\alpha}_m(x^{h,a}) \leq Q_m^{\max} \quad \forall m \in M, \tag{88}$$

which means, that the inner optimization model also has to be solved for all $m \in M$.

As solving two interleaved optimization models is not suitable for an ILP solver, we dualise the above optimization model, to be able to directly solve the heat flux limit constraint above. We introduce the variables u_m and v_m^h and obtain the dual optimization model for the respective measurement point m given by:

- **Objective function:**

$$\alpha_m(x^{h,a}) = \min \Gamma \cdot u_m + \sum_{h \in H} v_m^h$$

- **Decision variables:**

$$u_m \in \mathbb{R}_0^+$$
$$v_m^h \in \mathbb{R}_0^+ \quad \forall h \in H$$

- **Constraint:**
$$u_m + v_m^h \geq \sum_{a \in A} \hat{Q}_m^{h,a} \cdot x^{h,a} \quad \forall h \in H.$$

The constraint matrix of the inner optimization model is total unimodular thus the solution of the MILP $\alpha_m(x^{h,a})$ is equivalent to the solution of the initial ILP $\hat{\alpha}_m(x^{h,a})$. That said we can replace $\hat{\alpha}_m(x^{h,a})$ by $\alpha_m(x^{h,a})$ and obtain

$$\sum_{h \in H} \sum_{a \in A} Q_m^{h,a} \cdot x^{h,a} + \alpha_m(x^{h,a}) \leq Q_m^{\max} \quad \forall m \in M. \tag{89}$$

Now we can simplify the inner optimization model and obtain

$$\sum_{h \in H} \sum_{a \in A} Q_m^{h,a} \cdot x^{h,a} + \Gamma \cdot u_m + \sum_{h \in H} v_m^h \leq Q_m^{\max} \quad \forall m \in M \tag{90}$$

with the decision variables

$$u_m \in \mathbb{R}_0^+ \quad \forall m \in M \tag{91}$$
$$v_m^h \in \mathbb{R}_0^+ \quad \forall h \in H \quad \forall m \in M \tag{92}$$

and the constraint

$$u_m + v_m^h \geq \sum_{a \in A} \hat{Q}_m^{h,a} \cdot x^{h,a} \quad \forall h \in H \quad \forall m \in M. \tag{93}$$

This constraint now is directly solvable as an MILP.

4.3.3 Summarized optimization model

- **Definitions:**
$$Q_m^{\text{receiver}} = \sum_{h \in H} \sum_{a \in A} Q_m^{h,a} \cdot x^{h,a}$$
$$\hat{Q}_m^{h,a} = Q_{\text{worst},m}^{h,a} - Q_m^{h,a}$$

- **Objective function:**
$$\max Q^{\text{total}} = \sum_{m \in M} Q_m^{\text{receiver}}$$

- **Decision variables:**
$$x^{h,a} \in \{0,1\} \quad \forall h \in H \quad \forall a \in A$$
$$u_m \in \mathbb{R}_0^+ \quad \forall m \in M$$
$$v_m^h \in \mathbb{R}_0^+ \quad \forall h \in H \quad \forall m \in M$$

- **First constraint:**
$$\sum_{a \in A} x^{h,a} \leq 1 \quad \forall h \in H$$

- **Second constraint:**
$$\sum_{h \in H} \sum_{a \in A} Q_m^{h,a} \cdot x^{h,a} + \Gamma \cdot u_m + \sum_{h \in H} v_m^h \leq Q_m^{\max} \quad \forall m \in M$$

- **Third constraint:**
$$u_m + v_m^h \geq \sum_{a \in A} \hat{Q}_m^{h,a} \cdot x^{h,a} \quad \forall h \in H \quad \forall m \in M$$

5 Application

In this section we apply the deterministic and the robust aiming strategy to the solar tower power plant PS10 in Spain. In order to analyse the obtained solutions properly we look at the parameters affecting the outcome of the optimization problem first, before describing the parameter sets chosen for the application of the aiming strategies in this work. Lastly we discuss the results obtained for the previously described parameters sets.

5.1 Parameters

Parameters are the quantities that affect the outcome of the aiming point strategy, i.e. the choice of aiming points for each heliostat given by the decision variables $x^{h,a}$ as introduced in Section 3.1.4. Besides the constraints limiting the heat flux or the heat flux gradient, the obtained result is also influenced by the heliostat images provided by the optical model and by solver parameters.

5.1.1 Optical model

The following parameters can be adjusted to change the obtained heliostat images:

- Sun
  - $(\gamma_{\text{solar}}, \theta_{\text{solar}})$: the position of the sun as seen from the ground in polar coordinates
  - DNI: the irradiation strength specified as direct normal irradiation
- Heliostats
  - $(x, y, z)^h$ the position of a heliostat in our coordinate system as specified in Section 2
  - A^h: the total mirror area of a heliostat

- $\sigma^h_{\text{optical}}$: the optical error of a heliostat
- r^h: the reflectivity of a heliostat
- $\sigma^h_{\text{tracking,horizontal}}$,$\sigma^h_{\text{tracking,vertical}}$: the horizontal and vertical tracking error of a heliostat

- Receiver
  - the receiver type (rectangular, cylindric cavity, cylindric external)
  - w_{rec} or d_{rec}: the width or respectively the diameter of the receiver
  - h_{rec}: the height of the receiver
  - θ_{rec}: the tilt angle of a rectangular receiver
  - the existence and discretization of a heat shield at the receiver
  - h_{tower}: the height of the tower
  - h_{top}: the vertical distance from the top edge of the receiver to the top edge of the tower
  - $(n_{a,x},\, n_{a,y})$: the number of aim points in horizontal and vertical direction
  - $(n_{m,x},\, n_{m,y})$: the number of measurement points in horizontal and vertical direction

Note that the beam power $P^{h,a}$ reflected by one heliostat linearly depends on the DNI, A^h and r^h as specified by Equation (8). As these parameters are only used in this equation it is enough to adjust one of them.

Analogously it is enough to change h_{top} or h_{tower} as both heights only influence the coordinates of the receiver points.

5.1.2 Optimization problem

The following parameters can be adjusted to change the outcome of the optimization directly by adjusting the constraints:

- Deterministic aiming strategy
  - $Q^{\max}_m \quad \forall m \in M$: the heat flux limit
  - $G^{\max,\text{horizontal}}_{i-1,j} \quad \forall i \in \{2, ..., n_{m,x}\} \quad \forall j \in \{1, ..., n_{m,y}\}$: the horizontal heat flux gradient limit
  - $G^{\max,\text{vertical}}_{i,j-1} \quad \forall i \in \{1, ..., n_{m,x}\} \quad \forall j \in \{2, ..., n_{m,y}\}$: the vertical heat flux gradient limit

- Robust aiming strategy
  - $Q^{\max}_m \quad \forall m \in M$: the heat flux limit
  - Γ: the number of deviating heliostats

5.1.3 Solver

The following parameters can be adjusted to influence the behaviour of the solver:

- $t^{\max}$: the upper bound for the computation time
- ϵ: the relative gap between the current solution and the current upper bound

5.2 Parameters settings for the applications

In this work we apply the aiming strategies to the solar tower power plant PS10, thus every optical model parameter except the sun parameters and the receiver resolution are set. Technical data is taken from [14] and [15]. We use different constraint parameters and solver settings.

The parameter settings for the optical model are given in Table 1, for the optimization models in Table 2 and for the solver in Table 4.

The scaled heat flux profiles are given by the Figures 19a and 19b scaled by $Q^{\max} \cdot f$. The factor f is chosen by the method described in Section 3.7. It is given in Table 3.

We terminate the solution process by using upper bounds for the run time and do not use lower bounds for the optimality gap. $t_1^{\max}$ is an usual upper bound for taking cloud movements into account, $t_2^{\max}$ is an upper bound acceptable for running the optimization periodically for a clear sky szenario without clouds for different sun positions over the day.

5.3 Application cases

From the settings given in Section 5.2 we define the following application cases for the deterministic and the robust aiming strategy. The application cases for the deterministic aiming strategy are given in Table 5, the application cases for the robust aiming strategy in Table 6.

For every obtained solution we look at the gap ϵ and the value of the objective function i.e. the amount of thermal energy that is transferred to the receiver for both run times $t_1^{\max}$ and $t_2^{\max}$. The visualisations of the results show the obtained results for the longer run time except the solver found an optimal solution in a run time less or equal to $t_1^{\max}$.

Because the size of the robust optimization model is very large, it is not possible to build the constraint matrix for the fine resolution in Matlab on the used computer, as it would exceed the RAM. For this reason we only use the rough discretization for the robust aiming strategy.

Sun parameters	Setting 1 (morning)	Setting 2 (noon)
DNI	$700\frac{\mathrm{W}}{\mathrm{m}^2}$	$1050\frac{\mathrm{W}}{\mathrm{m}^2}$
γ_{solar}	$-45°$	$0°$
θ_{solar}	$40°$	$14°$
η_{aa}	computed by Equation (7)	computed by Equation (7)
σ_{sunshape}	2.51mrad	2.51mrad
Heliostat parameters	**Setting 1**	**-**
$(x, y, z)^h$	corresponding to the PS10 positions	-
A^h	121m	-
$\sigma^h_{\text{optical}}$	2.9mrad	-
r^h	0.97	-
$\sigma^h_{\text{tracking,horizontal}}$	1mrad	-
$\sigma^h_{\text{tracking,vertical}}$	1mrad	-
Receiver parameters	**Setting 1 (rough discr.)**	**Setting 2 (fine discr.)**
type	cylindric cavity	cylindric cavity
d_{rec}	14m	14m
h_{rec}	12m	12m
h_{tower}	120m	120m
h_{top}	7.5m	7.5m
heatshield	1m to each side	2m to each side
$(n_{a,x}, n_{a,y})$	(3,2)	(6,4)
$(n_{m,x}, n_{m,y})$	(6,4)	(12,8)
$(\text{ref}_x, \text{ref}_y)$	(4,4)	(2,2)

Table 1: Parameter settings for the optical model

Det. opt.	Setting 1	Setting 2	-	-
$Q^{\max}$	$800\frac{\mathrm{kW}}{\mathrm{m}^2}$ (constant)	scaled profile	-	-
$Q^{\max,\text{heat shield}}$	$0.4 \cdot Q^{\max}$	$0.4 \cdot Q^{\max}$	-	-
$G^{\max,\text{horizontal}}$	-	-	-	-
$G^{\max,\text{vertical}}$	$800\frac{\mathrm{kW}}{12\mathrm{m}}$	$800\frac{\mathrm{kW}}{12\mathrm{m}}$	-	-
Rob. opt.	**Setting 1**	**Setting 2**	**Setting 3**	**Setting 4**
$Q^{\max}$	$800\frac{\mathrm{kW}}{\mathrm{m}^2}$ (constant)	scaled profile	$800\frac{\mathrm{kW}}{\mathrm{m}^2}$ (constant)	scaled profile
$Q^{\max,\text{heat shield}}$	$0.4 \cdot Q^{\max}$	$0.4 \cdot Q^{\max}$	$0.4 \cdot Q^{\max}$	$0.4 \cdot Q^{\max}$
Γ	30	30	60	60

Table 2: Parameter settings for the optimization models

f	Rough discr.	Fine discr.	$\Gamma = 30$	$\Gamma = 60$
Morning	0.3	0.15	0.4	0.5
Noon	0.4	0.25	0.5	0.6

Table 3: Scaling factor for the relative receiver heat flux distributions

Solver parameters	Setting 1	Setting 2
$t^{\max}$	60s	30min
ϵ	-	-

Table 4: Parameters settings for the solver

Application case	Opt. mod. setting	Receiver setting	Det. opt. setting
1	morning	rough discr.	const. max heat flux
2	noon	rough discr.	const. max heat flux
3	morning	rough discr.	heat flux profile
4	noon	rough discr.	heat flux profile
5	morning	fine discr.	const. max heat flux
6	noon	fine discr.	const. max heat flux
7	morning	fine discr.	heat flux profile
8	noon	fine discr.	heat flux profile

Table 5: Parameters settings for the deterministic aiming strategy

Application case	Opt. mod. setting	Rob. opt. setting
1	morning	const. max heat flux, $\Gamma = 30$
2	noon	const. max heat flux, $\Gamma = 30$
3	morning	heat flux profile, $\Gamma = 30$
4	noon	heat flux profile, $\Gamma = 30$
5	morning	const. max heat flux, $\Gamma = 60$
6	noon	const. max heat flux, $\Gamma = 60$
7	morning	heat flux profile, $\Gamma = 60$
8	noon	heat flux profile, $\Gamma = 60$

Table 6: Parameters settings for the robust aiming strategy

5.4 Results

We solved the optimization models by using the Gurobi solver via the Matlab API using a computer with a 3.1 GHz processor and 16GB RAM. For the application cases defined in Section 5.3 we obtained the following results.

The choice of the horizontal aim points in the heliostat allocation figures is explained in the respective legends. The vertical aim point allocation is visualised by the brightness of the respective color. Dark colors represent low positions of the aim points on the receiver while bright colors represent high positions.

Mentioning previous application cases refers the current application case to the one of the respective section.

5.4.1 Deterministic aiming strategy

1 The visualisations of the results are almost identical for both run times. The solver terminates with the optimal solution after 329 seconds. The optimality gaps are given by $\epsilon(t_1^{\max}) = 1.223 \cdot 10^{-4}$ and $\epsilon(t_2^{\max}) = 0.999 \cdot 10^{-5}$. $4.010 \cdot 10^7$W and $4.011 \cdot 10^7$W thermal energy are transferred to the receiver in total respectively. The visualisation of the results for the longer run time is shown in Figure 21.

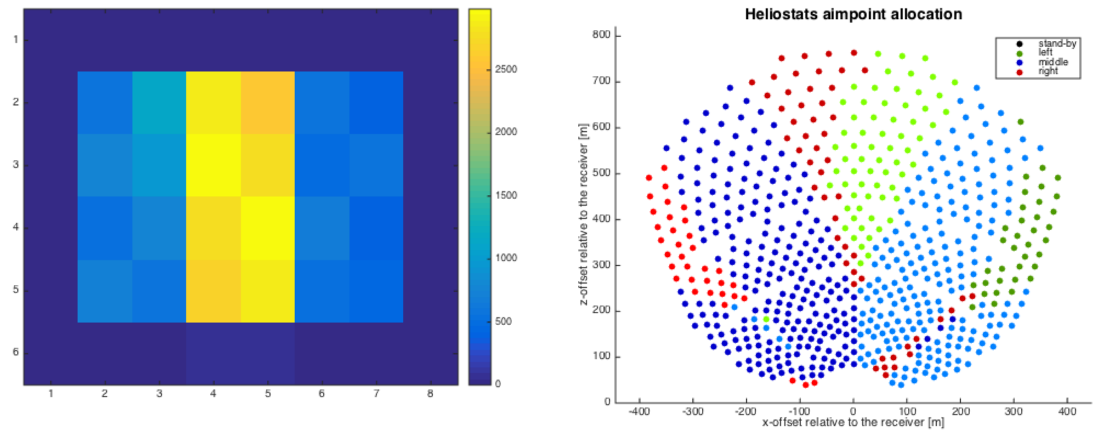

(a) Flux density at the receiver in kW per measurement point area

(b) Heliostat allocation

Figure 21: Results of the optimization model for the first application case of the deterministic aiming strategy for a run time of 329 seconds.

The majority of the heliostats targets the middle horizontal aim points, because the heat fluxes missing the receiver are minimal for such an aim point choice. Heliostats with large incidence angles in x-direction especially target aim points at the middle of the receiver. Their images are distorted the most when being projected onto the receiver surface, which means that these heliostats are most likely to miss the receiver with parts of their images.

If heliostats do not target the middle horizontal aim points, they target the aim points, for which the incidence angle of the sun rays onto the heliostat and thus the cosine losses are minimal.

As vertical gradients are constrained, the vertical heat flux difference between the middle horizontal measurement points must not exceed the defined maximum. This is achieved by distributing the heat fluxes between the lower and the upper aim point.

2 The visualisations of the results are almost identical for both run times. The solver does not terminate with an optimal solution. The optimality gaps are given by $\epsilon(t_1^{\max}) = 2.861 \cdot 10^{-4}$ and $\epsilon(t_2^{\max}) = 1.369 \cdot 10^{-4}$. $5.700 \cdot 10^7$W and $5.700 \cdot 10^7$W thermal energy are transferred to the receiver in total respectively. The visualisation of the results for the longer run time is shown in Figure 22.

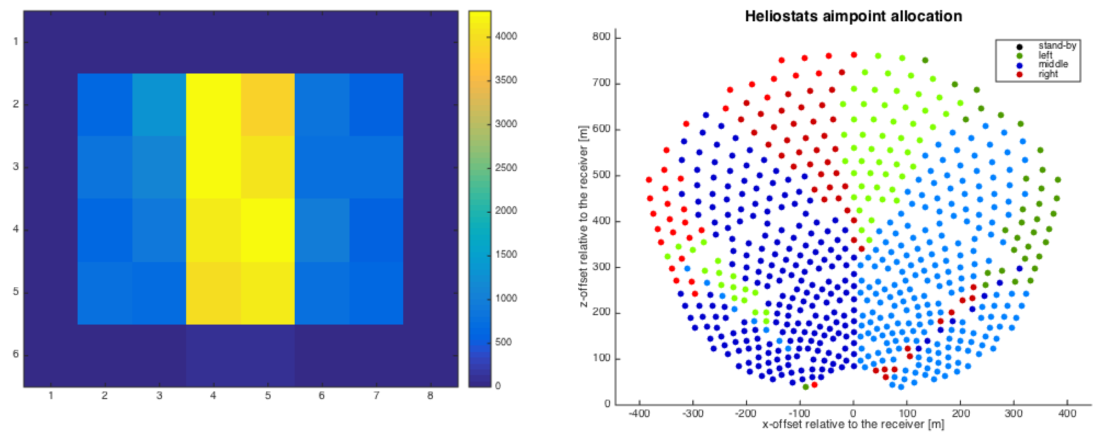

(a) Flux density at the receiver in kW per measurement point area

(b) Heliostat allocation

Figure 22: Results of the optimization model for the second application case of the deterministic aiming strategy for a run time of 30 minutes.

Analogously to the previous application case most of the heliostats target the middle horizontal aimpoints while distributing their heat fluxes between the upper and the lower aim point. It is visible that the heat flux density at the receiver is larger compared to the first application case. This is caused by the change of the sun position. At noon the DNI is higher and the cosine losses at the heliostats are smaller compared to a sun position at morning.

3 The visualisations of the results are identical for both run times. The solver does not terminate with an optimal solution. The optimality gaps are given by $\epsilon(t_1^{\max}) = 2.055 \cdot 10^{-4}$ and $\epsilon(t_2^{\max}) = 1.825 \cdot 10^{-4}$. $3.965 \cdot 10^7$W thermal energy are transferred to the receiver for each case in total. The visualisation of the results for the longer run time is shown in Figure 23.

Compared to the application cases 1 and 2, less heliostats target the middle horizontal aim points and more heliostats target the aim points located at the left or right hand

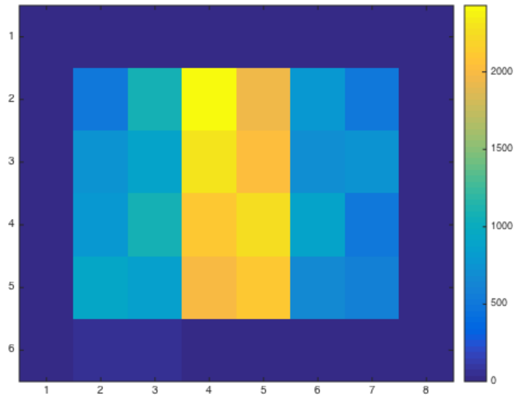

(a) Flux density at the receiver in kW per measurement point area

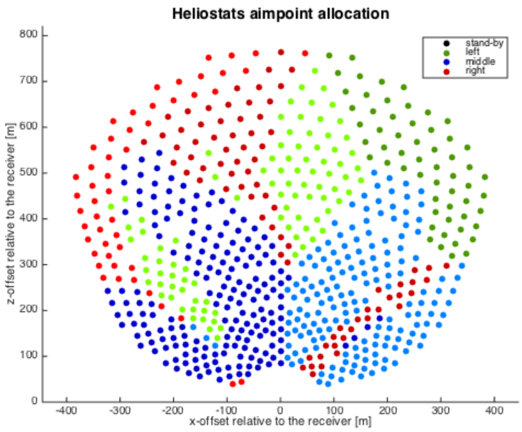

(b) Heliostat allocation

Figure 23: Results of the optimization model for the third application case of the deterministic aiming strategy for a run time of 30 minutes.

side of the receiver. This results in the heat flux density being weaker at the middle and being stronger at the sides of the receiver. Such an outcome is desired as it leads to the obtained heat flux distribution at the receiver being close to the one specified as maximum heat flux constraint.

4 The visualisations of the results are almost identical for both run times. The solver does not terminate with an optimal solution. The optimality gaps are given by $\epsilon(t_1^{\max}) = 1.309 \cdot 10^{-3}$ and $\epsilon(t_2^{\max}) = 2.790 \cdot 10^{-4}$. $5.433 \cdot 10^7$W and $5.439 \cdot 10^7$W thermal energy are transferred to the receiver in total respectively. The visualisation of the results for the longer run time is shown in Figure 24.

The heliostat allocation is relatively similar to the one in application case 3. The reason for this is, that the maximum heat flux constraint is scaled with a larger factor as the amount of thermal energy that is reflected by the heliostats is larger as well due to the changed sun position.

5 The visualisations of the results are almost identical for both run times. The solver does not terminate with an optimal solution. The optimality gaps are given by $\epsilon(t_1^{\max}) = 5.935 \cdot 10^{-4}$ and $\epsilon(t_2^{\max}) = 2.599 \cdot 10^{-4}$. $4.163 \cdot 10^7$W and $4.165 \cdot 10^7$W thermal energy are transferred to the receiver in total respectively. The visualisation of the results for the longer run time is shown in Figure 25.

The heliostat allocation is comparable with the one from application case 1 on a finer aim point grid: Most heliostats target aim points positioned at the middle of the receiver to minimize the amount of thermal energy missing it. In order to not violate

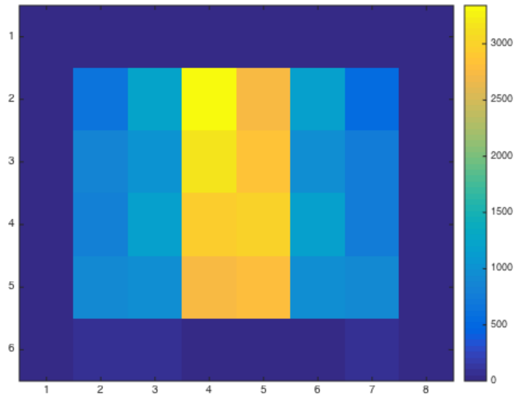

(a) Flux density at the receiver in kW per measurement point area

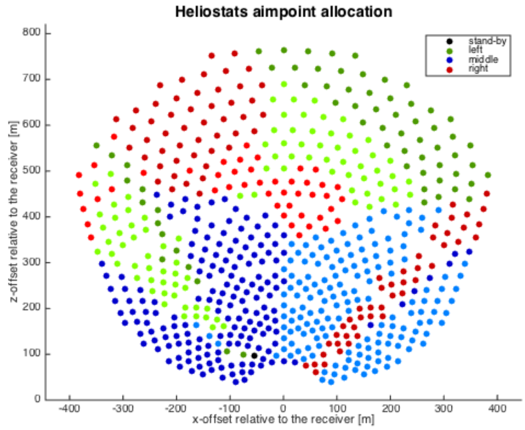

(b) Heliostat allocation

Figure 24: Results of the optimization model for the fourth application case of the deterministic aiming strategy for a run time of 30 minutes.

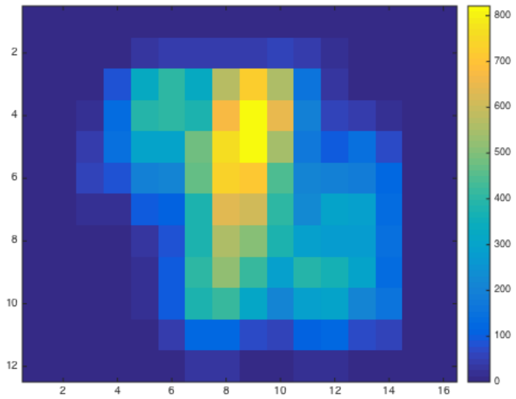

(a) Flux density at the receiver in kW per measurement point area

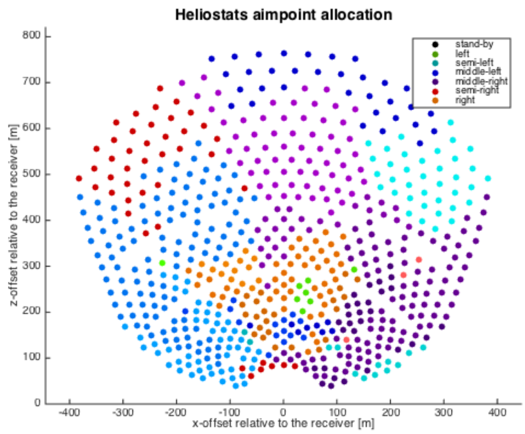

(b) Heliostat allocation

Figure 25: Results of the optimization model for the fifth application case of the deterministic aiming strategy for a run time of 30 minutes.

heat flux gradient constraints, the heat fluxes are distributed over the height of the receiver.

It is notable, that heliostats close to the tower with small incidence angles in x-direction target the aim points at the sides of the receiver as their distribution size is small due to the relatively short distance. That way thermal energy can be transferred to the sides of the receiver without much of it missing.

6 The visualisations of the results are almost identical for both run times. The solver does not terminate with an optimal solution. The optimality gaps are given by $\epsilon(t_1^{\max}) = 1.061 \cdot 10^{-3}$ and $\epsilon(t_2^{\max}) = 3.919 \cdot 10^{-4}$. $5.933 \cdot 10^7$W and $5.937 \cdot 10^7$W thermal energy are transferred to the receiver in total respectively. The visualisation of the results for the longer run time is shown in Figure 26.

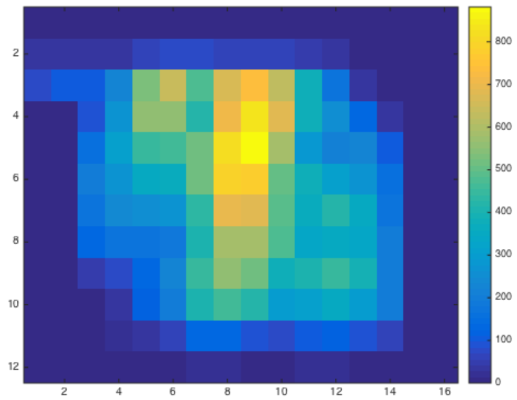

(a) Flux density at the receiver in kW per measurement point area

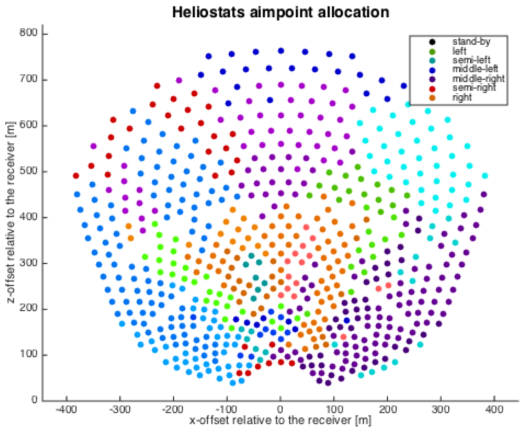

(b) Heliostat allocation

Figure 26: Results of the optimization model for the sixth application case of the deterministic aiming strategy for a run time of 30 minutes.

Compared to application case 5 there is a larger amount of thermal energy available to be distributed at the receiver surface. Contrary to the application cases 1 and 2 the obtained relative heat flux distribution changes rather then looking similar with the intensity being scaled up.

The available thermal energy is spread over the receiver surface in a more homogeneous fashion. The heliostat allocation changes accordingly: less heliostats target aim points at the middle of the receiver and more heliostats target aim points at the sides. Again the left and right aim points are targeted by heliostats in front of the tower with small incidence angles in x-direction.

7 The visualisations of the results are identical for both run times. The solver does not terminate with an optimal solution. The optimality gaps are given by $\epsilon(t_1^{\max}) = 1.387 \cdot 10^{-3}$ and $\epsilon(t_2^{\max}) = 1.019 \cdot 10^{-3}$. $3.929 \cdot 10^7$W and $3.930 \cdot 10^7$W thermal energy are transferred to the receiver in total respectively. The visualisation of the results for the longer run time is shown in Figure 27.

The known groups of heliostats target the respective aimpoints at the receiver as discussed in the previous application cases.

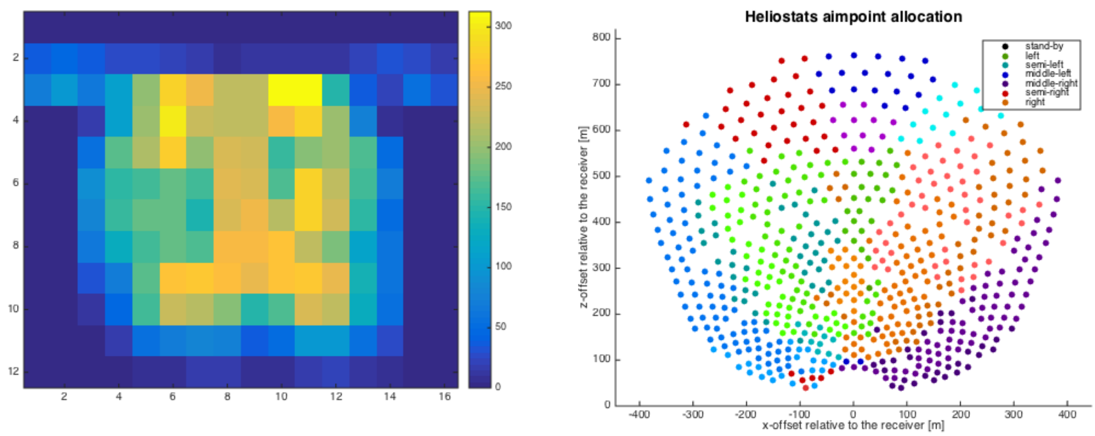

(a) Flux density at the receiver in kW per measurement point area

(b) Heliostat allocation

Figure 27: Results of the optimization model for the seventh application case of the deterministic aiming strategy for a run time of 30 minutes.

Obtaining a complex distribution perfectly as desired is difficult when a certain run time is required. If the scaling factor of the distribution is too large, the model can be solved in an appropriate amount of time but only approximates the desired distribution. Such an result is shown in Figure 27a.

If the scaling factor is chosen too small, we most likely can get very close to the desired distribution but may have heliostats not targeting aim points. Additionally we need a large amount of time for solving the optimization problem. The latter problem even occurs for a perfectly chosen scaling factor.

As we restrict the run time of the solver in order to investigate the applicability of the aiming strategies to real solar tower power plants, we only can approximate the desired heat flux distribution.

8 The visualisations of the results are almost identical for both run times. The solver does not terminate with an optimal solution. The optimality gaps are given by $\epsilon(t_1^{\max}) = 2.420 \cdot 10^{-3}$ and $\epsilon(t_2^{\max}) = 8.182 \cdot 10^{-4}$. $5.752 \cdot 10^7$W and $5.761 \cdot 10^7$W thermal energy are transferred to the receiver in total respectively. The visualisation of the results for the longer run time is shown in Figure 28.

The receiver heat flux distribution and the heliostat allocation are relatively similar to the ones of application case 7, except that the heat fluxes hitting the receiver are higher due to the sun position being noon.

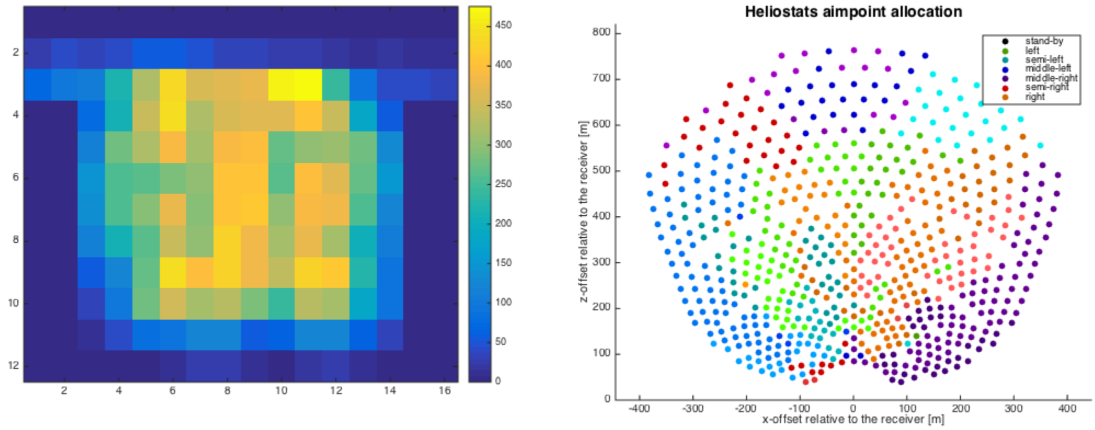

(a) Flux density at the receiver in kW per measurement point area

(b) Heliostat allocation

Figure 28: Results of the optimization model for the eighth application case of the deterministic aiming strategy for a run time of 30 minutes.

5.4.2 Robust aiming strategy

1 The solver terminates with the optimal solution after 6.5 seconds. The optimality gap is given by $\epsilon(t_1^{\max}) = 0$. $4.194 \cdot 10^7$W thermal energy are transferred to the receiver in total. The visualisation of the results is shown in Figure 29.

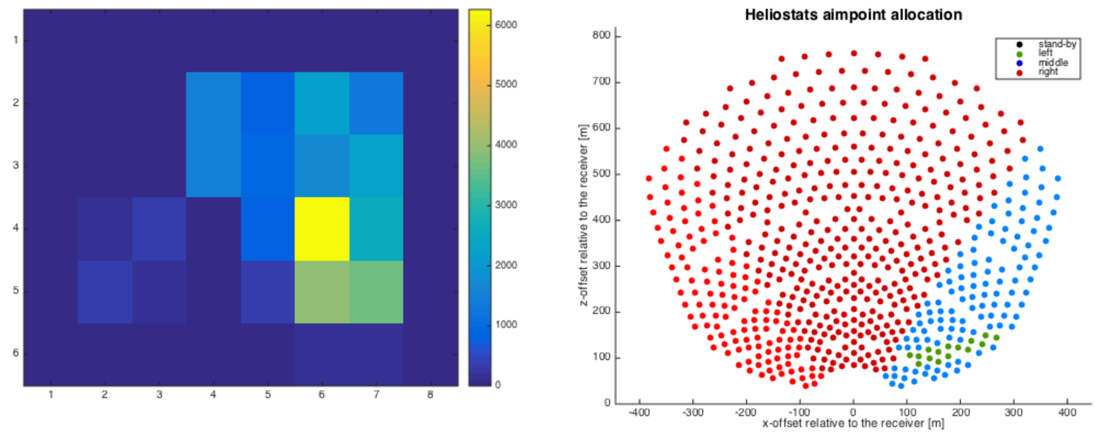

(a) Flux density at the receiver in kW per measurement point area

(b) Heliostat allocation

Figure 29: Results of the optimization model for the first application case of the robust aiming strategy for a run time of 6.5 seconds.

No heat flux gradients are constrained, thus every heliostat targets the point for which its maximum heat flux is transferred to the receiver. As the receiver can withstand a very high maximum heat flux, almost every heliostat can target the same aim point without violating a safety constraint as the DNI of the sun is relatively low at morning.

For this application case the main factors determining the differences in the thermal energies reflected by the heliostats are the incidence angles of the sun rays hitting the mirrors, as they specify the effect of the cosine losses of the heliostats. The PS10 solar tower power plant is located on the northern hemisphere, thus the sun is positioned eastern at morning, which corresponds the positive x-direction in Figure 29b. For such a sun position the cosine losses of the heliostats are minimized when most of them target the right aim points.

2 The solver terminates with the optimal solution after 9.6 seconds. The optimality gap is given by $\epsilon(t_1^{\max}) = 3.776 \cdot 10^{-7}$. $6.104 \cdot 10^7$W thermal energy are transferred to the receiver in total. The visualisation of the results is shown in Figure 30.

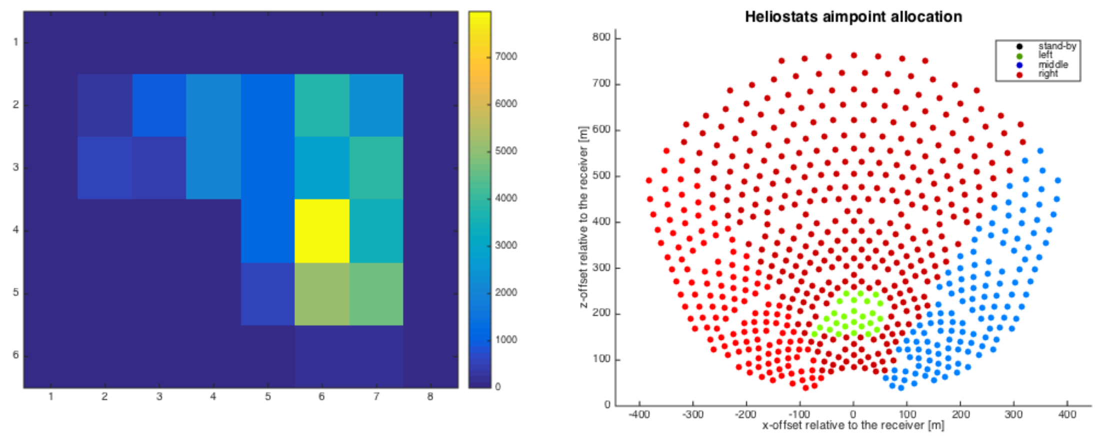

(a) Flux density at the receiver in kW per measurement point area

(b) Heliostat allocation

Figure 30: Results of the optimization model for the second application case of the robust aiming strategy for a run time of 9.6 seconds.

At noon the heat fluxes of the heliostats are large enough, that all images combined could lead to a violation of the maximum heat flux constraint.

The heliostats represented by the green dots in Figure 30b can concentrate the largest amounts of thermal energy onto the bottom right aim point. Their distribution sizes are small due to the small distances between them and the tower. Furthermore they are hardly distorted due to the small incidence angles in x- and y-direction.

To prevent the violation of the maximum heat flux constraint, these heliostats target the aim point, which is furthest away from the critical point. As the critical point is the measurement point at the position of the lower right aim point, the point furthest away is the aim point in the top left corner of the receiver.

3 The solver terminates with the optimal solution after 17.0 seconds. The optimality gap is given by $\epsilon(t_1^{\max}) = 9.900 \cdot 10^{-5}$. $4.180 \cdot 10^7$W thermal energy are transferred to the receiver in total. The visualisation of the results is shown in Figure 31.

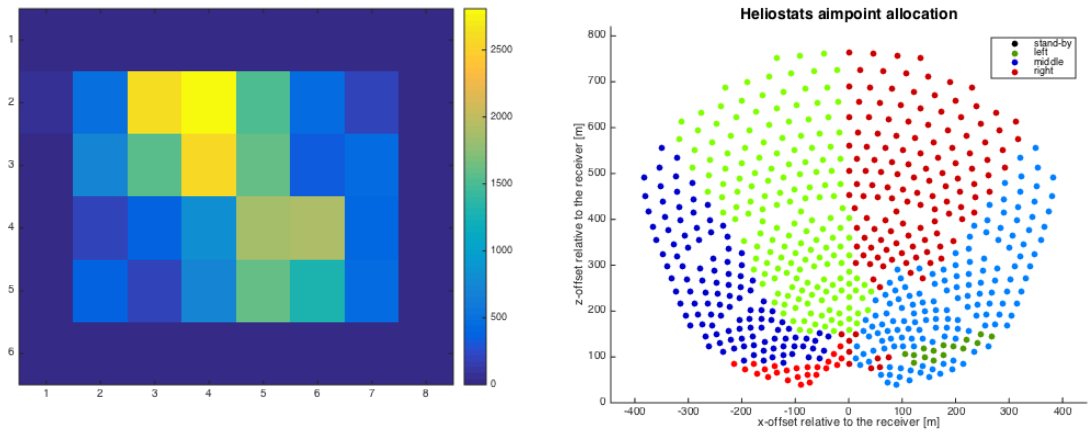

(a) Flux density at the receiver in kW per measurement point area

(b) Heliostat allocation

Figure 31: Results of the optimization model for the third application case of the robust aiming strategy for a run time of 17.0 seconds.

As observed for the deterministic application cases with a given heat flux distribution, the heat fluxes are distributed more evenly over the receiver area. Accordingly the heliostats target different aimpoints with the concepts discussed for all of the previous application cases.

The center of the receiver is a critical area at which maximum heat flux constraints could be violated, because heliostats from the left and the right hand side of the receiver could deviate towards the middle. As the robust aiming strategy is more conservative than the deterministic one, the number of heliostats targeting middle horizontal aim points is smaller then for the deterministic aiming strategy as shown in Figure 23b.

4 The solver terminates with the optimal solution after 60.2 seconds. The optimality gap is given by $\epsilon(t_1^{\max}) = 2.650 \cdot 10^{-4}$. $6.063 \cdot 10^7$W thermal energy are transferred to the receiver in total. The visualisation of the results is shown in Figure 32.

The heat flux distribution at the receiver and the heliostat allocation at noon are analogous to application case 3. As described there, violations of the maximum heat

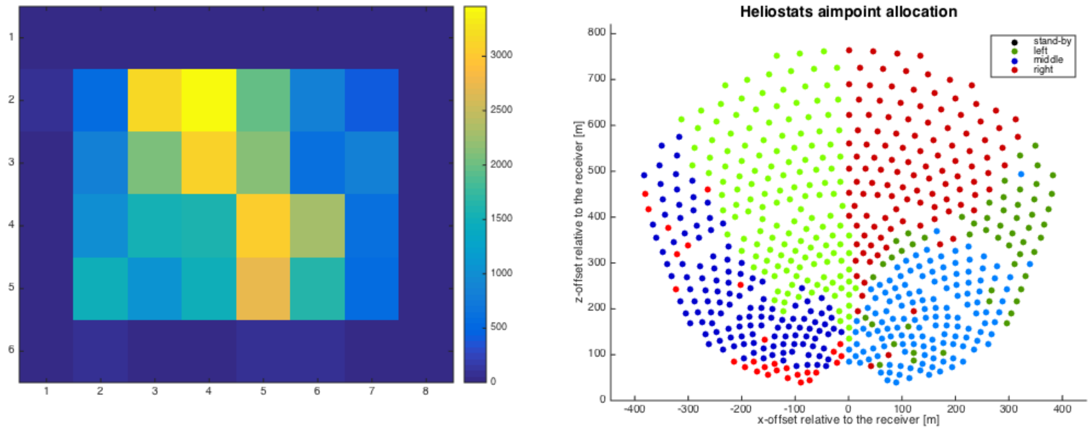

(a) Flux density at the receiver in kW per measurement point area

(b) Heliostat allocation

Figure 32: Results of the optimization model for the fourth application case of the robust aiming strategy for a run time of 60.2 seconds.

flux constraints are most likely to occur at the middle area of the receiver. To prevent that from happening, some heliostats, that usually would target middle horizontal aim points, target the left or right aim points now. They are represented as single red or green dots in Figure 32b.

5 The solver terminates with the optimal solution after 61.2 seconds. The optimality gap is given by $\epsilon(t_1^{\max}) = 0$. $4.194 \cdot 10^7$W thermal energy are transferred to the receiver in total. The visualisation of the results is shown in Figure 33.

The heat flux distribution at the receiver and the heliostat allocation are analogous to application case 1.

6 The solver terminates with the optimal solution after 11.1 seconds. The optimality gap is given by $\epsilon(t_1^{\max}) = 3.737 \cdot 10^{-6}$. $6.103 \cdot 10^7$W thermal energy are transferred to the receiver in total. The visualisation of the results is shown in Figure 34.

The heat flux distribution at the receiver and the heliostat allocation are analogous to application case 2. However, it is noticeable, that the number of heliostats targeting the aim point that is furthest away from the bottom right aim point is larger due to the number of deviating heliostats Γ being larger. To prevent the violation of the maximum heat flux constraint, some heliostats even must not target an aim point at all.

7 The solver terminates with the optimal solution after 58.8 seconds. The optimality gap is given by $\epsilon(t_1^{\max}) = 9.022 \cdot 10^{-5}$. $4.179 \cdot 10^7$W thermal energy are transferred to

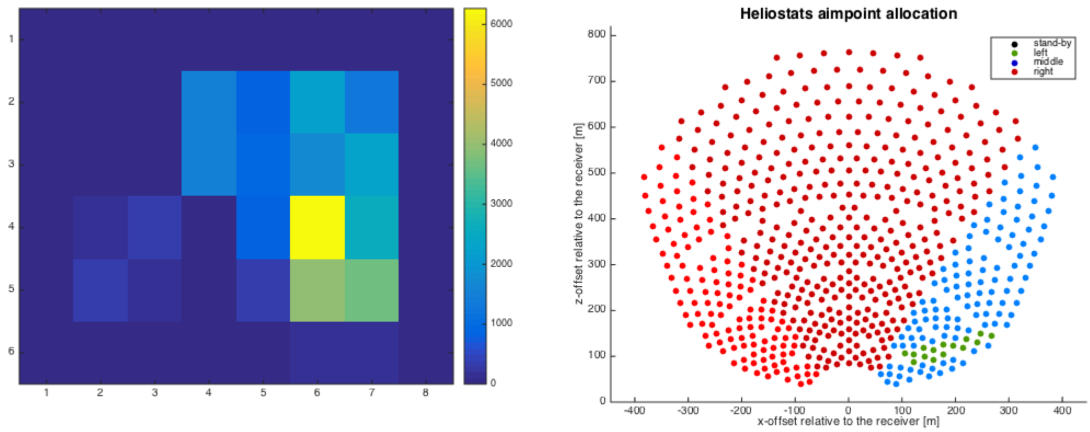

(a) Flux density at the receiver in kW per measurement point area

(b) Heliostat allocation

Figure 33: Results of the optimization model for the fifth application case of the robust aiming strategy for a run time of 61.2 seconds.

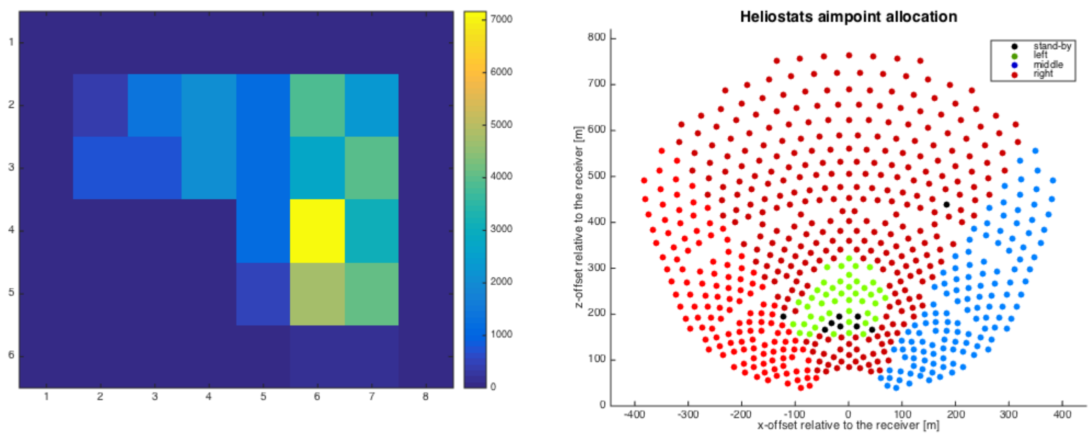

(a) Flux density at the receiver in kW per measurement point area

(b) Heliostat allocation

Figure 34: Results of the optimization model for the sixth application case of the robust aiming strategy for a run time of 11.1 seconds.

the receiver in total. The visualisation of the results is shown in Figure 35.

The heat flux distribution at the receiver and the heliostat allocation are analogous to application case 3. As the number of deviating heliostats is larger for this application case, some heliostats additionally target the aim points at the sides of the receiver instead of the aim points at the middle to prevent that the maximum heat flux constraint is violated. These heliostats are represented by the red dots at the left hand

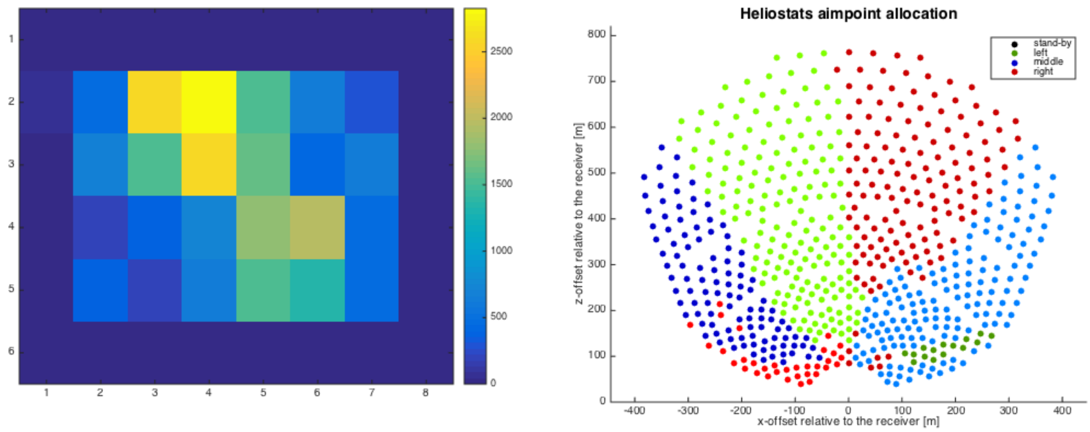

(a) Flux density at the receiver in kW per measurement point area

(b) Heliostat allocation

Figure 35: Results of the optimization model for the seventh application case of the robust aiming strategy for a run time of 58.8 seconds.

side of the heliostat field in Figure 35b.

8 The solver terminates with the optimal solution after 60.7 seconds. The optimality gap is given by $\epsilon(t_1^{\max}) = 1.348 \cdot 10^{-3}$. $6.047 \cdot 10^7$W thermal energy are transferred to the receiver in total. The visualisation of the results is shown in Figure 36.

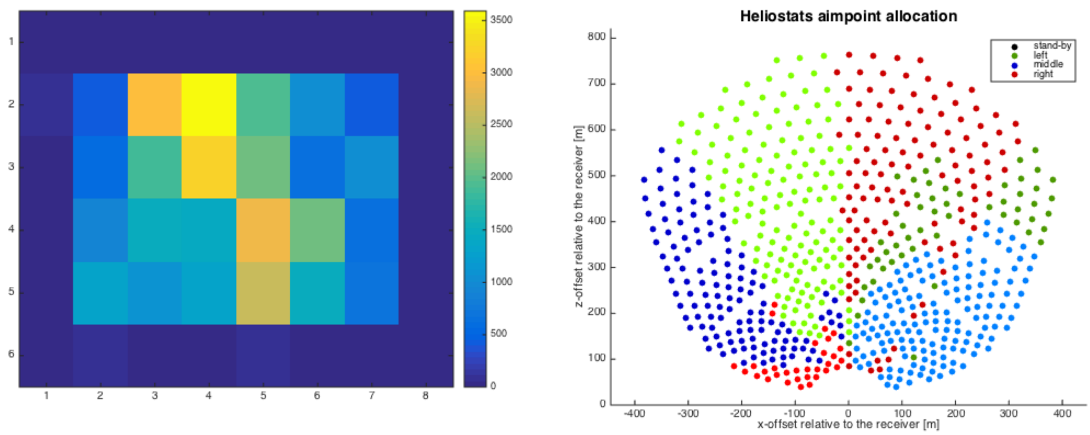

(a) Flux density at the receiver in kW per measurement point area

(b) Heliostat allocation

Figure 36: Results of the optimization model for the eighth application case of the robust aiming strategy for a run time of 60.7 seconds.

The heat flux distribution at the receiver and the heliostat allocation are analogous to application case 4 with differing positions of the deviating heliostats.

6 Conclusion and Outlook

Two realistically applicable aiming strategies were developed and applied to the PS10 solar tower power plant in Spain. An optical model capable of distorting heliostat images for three different receiver geometries was implemented to generate data for the optimization models.

The deterministic optimization model constrains the heat fluxes as well as the heat flux gradients. The robust optimization model constrains the heat fluxes and considers the tracking errors of heliostats. Both aiming strategies benefit the efficiency of the solar tower power plant by optimizing the amount of thermal energy that is transferred to the receiver as well as ensuring a long lifespan of the receiver by avoiding that heat fluxes or gradients exceed certain limits.

6.1 Comparison of the aiming strategies

When comparing the deterministic and the robust aiming strategy, several aspects are noticeable.

Firstly it is apparent – when comparing the run times of the aiming strategies – that considering heat flux gradient limits is very expensive. The problem size of the robust optimization model is a lot larger than the problem size of the deterministic model due to having both more decision variables and more constraints. Regardless of that, the robust model can be solved in close to real time whereas the optimal solution of the deterministic model in most cases cannot be found under 30 minutes of run time.

An important observation regarding that fact is though, that very good approximations of the optimal solution with a very small optimality gap can be found in close to real time for the deterministic aiming strategy. This qualifies both aiming strategies to account for cloud movements for an appropriate receiver discretization.

It is possible for both aiming strategies to approximate desired heat flux profiles. Considering heat flux gradients is helpful to obtain typical desired heat flux distributions as they lead to more homogeneous heat flux distributions in general. Furthermore the robust aiming strategy is more conservative, which means that a specific desired heat flux distribution is never going to be obtained perfectly.

For these reasons the deterministic aiming strategy is useful for accurately approximating a desired receiver heat flux distribution. The robust aiming strategy on the other hand can be used, when it is of exceptional importance, that certain heat flux values are not exceeded. Nevertheless one should use simple heat flux distributions as constraints to avoid obtaining very inhomogeneous distributions.

6.2 Outlook

The following can be done to continue this work:

- A more comprehensive analysis of the effects of the parameters in Section 5.1 on the solution of the optimization problems can be done to obtain deeper knowlegde of well suitable parameter choices so that solutions can be computed as fast as possible while maintaining an appropriate accuracy by using the respective receiver discretization.
- Robust gradient constraints can be included into the robust optimization model, to obtain an even more realistic and robust aiming strategy.
- The aiming strategies can be extended to not only maximize the amount of thermal energy hitting the receiver but also actively minimize the difference to a given receiver heat flux distribution.
- Different Γ values for each measurement point can be used to obtain even higher levels of robustness at critical areas at the receiver.

References

[1] Coating of heliostats. http://www.dlr.de/sf/desktopdefault.aspx/tabid-10436/20174_read-46859, 2018. Accessed: 19.07.18.

[2] Gemasolar tower power plant. https://csirosolarthermal.wordpress.com/tag/heliostat/, 2018. Accessed: 14.07.18.

[3] Renewables 2017 global status report. http://www.ren21.net/wp-content/uploads/2017/06/17-8399_GSR_2017_Full_Report_0621_Opt.pdf, 2018. Accessed: 19.07.18.

[4] Key numbers for solar tower plants. http://www.bine.info/publikationen/themeninfos/publikation/solarthermische-kraftwerke-2/turmkraftwerk-buendelt-sonne-punktgenau/?cHash=8aa0001eb1dade325e6cb1b120f8a7f6&type=333, 2018. Accessed: 19.07.18.

[5] Thomas Ashley, Emilio Carrizosa, and Enrique Fernández-Cara. Optimisation of aiming strategies in solar power tower plants. *Energy*, 137:285–291, 2017.

[6] Marco Astolfi, Marco Binotti, Simone Mazzola, Luca Zanellato, and Giampaolo Manzolini. Heliostat aiming point optimization for external tower receiver. *Solar Energy*, 157:1114–1129, 2017.

[7] Boris Belhomme, Robert Pitz-Paal, and Peter Schwarzbözl. Optimization of heliostat aim point selection for central receiver systems based on the ant colony optimization metaheuristic. *Journal of solar energy engineering*, 136(1):011005, 2014.

[8] Dimitris Bertsimas and Melvyn Sim. The price of robustness. *Operations research*, 52(1):35–53, 2004.

[9] Saeb M Besarati, D Yogi Goswami, and Elias K Stefanakos. Optimal heliostat aiming strategy for uniform distribution of heat flux on the receiver of a solar power tower plant. *Energy Conversion and Management*, 84:234–243, 2014.

[10] TA Dellin, MJ Fish, and CL Yang. User's manual for delsol2: a computer code for calculating the optical performance and optimal system design for solar-thermal central-receiver plants. Technical report, Sandia National Labs., Albuquerque, NM (USA); Sandia National Labs., Livermore, CA (USA), 1981.

[11] LA Díaz-Félix, M Escobar-Toledo, J Waissman, N Pitalúa-Díaz, and CA Arancibia-Bulnes. Evaluation of heliostat field global tracking error distributions by monte carlo simulations. *Energy procedia*, 49:1308–1317, 2014.

[12] John A Duffie and William A Beckman. *Solar engineering of thermal processes.* John Wiley & Sons, 2013.

[13] PL Leary and JD Hankins. User's guide for mirval: a computer code for comparing designs of heliostat-receiver optics for central receiver solar power plants. Technical report, Sandia National Laboratories (SNL-CA), Livermore, CA (United States), 1979.

[14] Corey J Noone, Manuel Torrilhon, and Alexander Mitsos. Heliostat field optimization: A new computationally efficient model and biomimetic layout. *Solar Energy*, 86(2):792–803, 2012.

[15] Rafael Osuna, Rafael Olavarrıa, Rafael Morillo, Marcelino Sánchez, Felipe Cantero, Valerio Fernández-Quero, Pedro Robles, T López, Antonio Esteban, Francisco Céron, et al. Ps10, construction of a 11mw solar thermal tower plant in seville, spain. In *Solar-PACES Conference, Seville, Spain, June*, pages 20–23, 2006.

[16] CL Pitman and LL Vant-Hull. Atmospheric transmission model for a solar beam propagating between a heliostat and a receiver. *Proc. Annu. Meet.-Am. Sect. Int. Sol. Energy Soc.;(United States)*, 5(CONF-820629-Vol. 5-Pt. 2), 1982.

[17] Pascal Richter, Manuel J Castro Diaz, Martin Frank, and Siegfried Müller. Simulation and optimization of solar thermal power plants. Technical report, Lehr-und Forschungsgebiet Simulation in der Kerntechnik, 2017.

[18] Mark Schmitz, Peter Schwarzbözl, Reiner Buck, and Robert Pitz-Paal. Assessment of the potential improvement due to multiple apertures in central receiver systems with secondary concentrators. *Solar Energy*, 80(1):111–120, 2006.

[19] Peter Schwarzbözl, Robert Pitz-Paal, and Mark Schmitz. Visual hflcal-a software tool for layout and optimisation of heliostat fields. In *Proceedings*, 2009.